Droplet 3D Cryobioprinting for Fabrication of Free-Standing and Volumetric Structures

Joshua Weygant,¹ Ali Entezari,[†] Fritz Koch,[†] Ricardo André Galaviz,[†] Carlos Ezio Garciamendez, Pável Hernández, Vanessa Ortiz, David Sebastián Rendon Ruiz, Francisco Aguilar, Andrea Andolfi, Ling Cai, Sushila Maharjan, Anayancy Osorio, Yu Shrike Zhang^{*}

J. Weygant, Dr. F. Koch, R.A. Galaviz, Dr. A. Entezari, C. E. Garciamendez, P. Hernández, V. Ortiz, D. S. Rendón Ruiz, F. Aguilar, A. Andolfi, L. Cai, Dr. S. Maharjan, Prof. Y. S. Zhang Division of Engineering in Medicine, Department of Medicine, Brigham and Women's Hospital, Harvard Medical School, Cambridge, MA 02139, USA

*Email: yszhang@bwh.harvard.edu

Dr. F. Koch, Prof. A. Osorio

Laboratory for Bioinspired Materials for Biomedical Engineering, IMTEK - Department of Microsystems Engineering, University of Freiburg, 79110 Freiburg, Germany

Dr. A. Entezari

School of Biomedical Engineering, University of Technology Sydney, NSW, 2007, Australia

A. Andolfi

Department of Informatics, Bioengineering, Robotics and Systems Engineering (DIBRIS), University of Genova, Genova, Italy

[†]A. Entezari, F. Koch, and R. A. Galaviz contributed to this work equally

¹J. Weygant is now at the Department of Engineering, University of Cambridge, CB2 1PZ Cambridge, United Kingdom

Abstract

Droplet-based bioprinting has shown remarkable potential in tissue engineering and regenerative medicine. However, it requires bioinks with low viscosities, which makes it challenging to create complex three-dimensional structures and spatially pattern them with different materials. This study introduces a novel approach to bioprinting sophisticated volumetric objects by merging droplet-based bioprinting and cryobioprinting techniques. By leveraging the benefits of cryopreservation, we fabricate, for the first time, intricate, self-supporting cell-free or cell-laden structures with single or multiple materials in a simple droplet-based bioprinting process that is facilitated by depositing the droplets onto a cryoplate followed by crosslinking during revival. We demonstrate the feasibility of this approach by bioprinting several cell types, with cell viability increasing to 80-90% after up to 2 or 3 weeks of culture. Furthermore, we showcase the applicational capabilities of this approach by bioprinting an endothelialized breast cancer model. Our results indicate that merging droplet and cryogenic bioprinting complements current droplet-based bioprinting techniques and opens new avenues for the fabrication of volumetric objects with enhanced complexity and functionality, presenting exciting potential for biomedical applications.

Keywords: 3D bioprinting, inkjet, droplet printing, cryogenic bioprinting, biofabrication, tissue engineering

1. Introduction

In recent years, three-dimensional (3D) bioprinting has emerged as an enabling technology to fabricate sophisticated structures containing biological materials or living cells.^[1,2] Various bioprinting methods have been developed, such as extrusion, [2-6] droplet-based, [7-9] vatphotopolymerization, [10–17] and more. Among these, droplet-based bioprinting has been established as one of the first bioprinting techniques and has been used to pattern cells as well as biocompatible materials.^[18] Compared to other techniques, droplet-based approaches feature several advantages, such as good resolution, non-contact mode, high throughput, usually low cost, and, depending on the cell type and the printing modality, it yields high cell viabilities of 70-90%. [8] To accommodate the different applications, droplet-based bioprinting can be used to bioprint either single cells^[19] or high cell densities (up to 7×10^7 cells mL⁻¹), which yields spheroid-like behavior of the deposited aggregates.^[20,21] The technique has been applied to bioprint various tissues, for example, bone,^[22] kidney,^[21] neuronal tissue,^[23] or vasculature.^[24,25] among others. Despite these advantages, droplet-based bioprinting has several disadvantages, such as limited bioink selection, low flow rates, and clogging of the orifice. One of the major drawbacks is that it requires bioinks with low viscosities, [26,27] due to which the bioprinted structures are non-self-supportive and lack structural integrity.[26-28]

While complex structures have been fabricated via laser-assisted bioprinting (LAB), it requires rapid gelation kinetics when fabricating structures with high shape fidelity and final structures may have metal residues in them. [29,30] Microvalve and inkjet approaches are cheaper but frequently require a crosslinking step after each layer due to the wetting and spreading of droplets, making it demanding and complicated to bioprint sophisticated 3D patterns. [7,31,32] Therefore, fabricating free-standing, self-supporting structures is one of the significant challenges in droplet-based bioprinting and usually requires complex workarounds. For example, a previous study crosslinked an alginate-based bioink with calcium by adjusting two nozzles, one ejecting the bioink, the other one the crosslinking agent, so that the droplets merged in flight, which was used for the fabrication of 3D-printed alginate constructs. [33] Another established method is printing of droplets into or onto a support bath containing a crosslinking solution, which enabled the fabrication of 3D objects. [34-36]

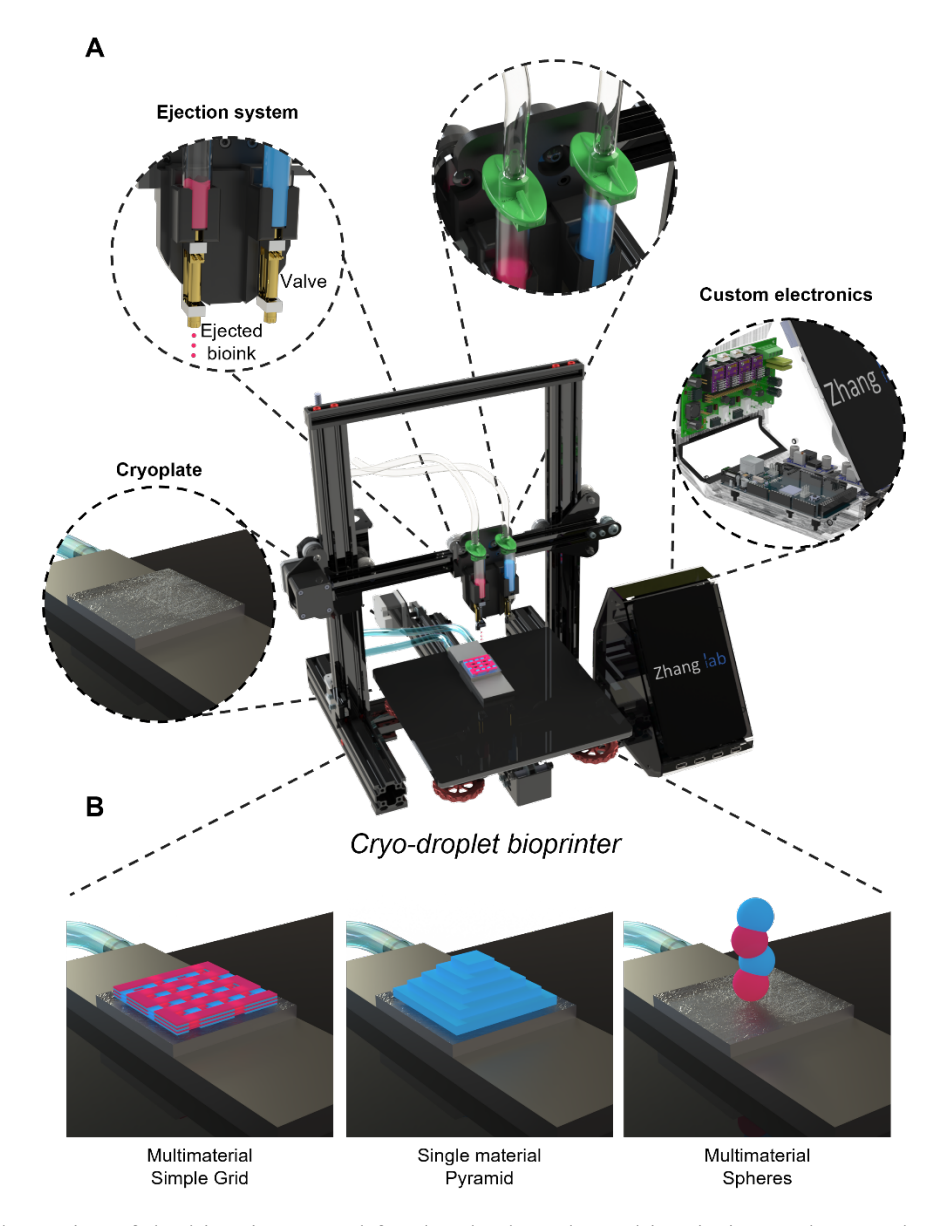


Figure 1. Schematics of the bioprinter used for droplet-based cryobioprinting and examples of achievable structures. (A) Schematic representation of the in-house-built system for droplet-based cryobioprinting. (B) Sophisticated, multi-material structures, fabricated via droplet-based cryobioprinting.

Due to these reasons, researchers utilizing droplet-based bioprinting approaches are often limited to depositing cells with culture media onto pre-prepared hydrogels.^[8,32] Recently, techniques were reported that combined inkjet printing of pure water and a freezing plate to produce complex 3D ice structures,^[37,38] overcoming some of the general challenges of droplet printing. However, these studies did not use hydrogels, nor did they include cells in their constructs. In parallel, we have developed a novel bioprinting technique that we termed cryobioprinting,

which entailed the deposition of cell-laden cryoprotective bioink through extrusion onto a cryoplate and immediate freezing of the bioprinted structures, to enhance shape fidelity as well as to allow shelf-ready storage of the cryobioprinted tissues.^[39,40] Here, for the first time, we report a technique that merges droplet-based bioprinting and cryobioprinting to enable the fabrication of free-standing, single- or multi-material, 3D architectures made of low-viscosity cell-laden bioinks in a single step.

For the present study, an in-house bioprinter was developed, shown in **Figure 1A**. The bioprinter was equipped with two microvalves that allowed for parallel ejection of multiple materials (**Figure 1B**). These valves were connected to an external air-pressure system, and custom-developed electronics controlled the bioprinter. To overcome the challenge of low-viscosity materials spreading over the substrate, the droplets were ejected onto a cryoplate, resulting in immediate freezing and preservation of the bioink's structural integrity. This advancement facilitated the straightforward patterning of complex, 3D structures, such as a pyramid (see **Figure 1B**). In addition, incorporating a second valve enabled the structuring of multi-material structures simply by ejecting a different material. This feature allowed the uncomplicated fabrication of structures such as multi-material grids or free-standing patterns (compare **Figure 1B**).

For bioprinting purposes, the frozen constructs were immediately crosslinked after bioprinting and subsequently transferred into cell-culture media. In this study, we showcased the capabilities of our approach by successfully bioprinting various cell types and analyzing their behaviors up to 14 days post-bioprinting. Furthermore, we employed the multi-material approach to create a vascularized breast cancer model, demonstrating the proof-of-concept versatility and potential of droplet-based cryobioprinting.

2. Results and Discussion

2.1. Droplet size characterizations

First, we characterized the sizes of the hydrogel-precursor droplets dispensed with the microvalve. Since droplet-based bioprinting requires low-viscosity materials, 7.5% (w/v) gelatin methacryloyl (GelMA) based on gelatin from fish skin was chosen for the bioink material because of its low viscosity and favorable compatibility with cells. [41,42] While GelMA is often derived from other sources (porcine, bovine), they display rheological properties such as higher viscosity

and gelation close to room temperature that are unsuitable for droplet-based bioprinting.^[43] Based on a previous study in which we systematically investigated the influence of cryoprotective agents for their use in cryobioprinting, 8% (w/v) melezitose and 10% (v/v) dimethyl sulfoxide (DMSO) were added to formulate the bioink.^[39,40] In addition, due to its cryoprotective properties,^[44] 10% (v/v) fetal bovine serum (FBS) was further added to the bioink.

The sizes of the hydrogel droplets dispensed from the microvalve and the stability of droplet generation were analyzed by varying the applied pressure as well as the opening time of the valve. Pressures of 100, 200, and 300 mbar and opening times of 500, 600, and 700 µs were applied. Resulting droplet volumes, which are in the lower range of previously reported volumes, [45] are shown in **Figure 2A**. As expected, the smallest droplets were generated with the shortest opening time of 500 µs and the lowest applied pressure of 100 mbar, whereas the largest droplets were generated with the longest opening times of 700 µs and the largest applied pressure of 300 mbar. For an opening time of 600 µs and 100 mbar, as well as for an opening time of 700 µs and applied pressures of 100 and 200 mbar, the generation of droplets was not stable because the orifice of the valve began to wet within the experiments, which led to no further droplets being formed. It was possible that these parameters led to an unstable generation of droplets since a larger opening time would allow for a larger volume of liquid to travel through the valve, which required higher applied energy for droplet formation. However, the generation of droplets from microvalves is highly complex and has been described in detail previously. [46,47] For the other parameters, the orifice did not wet and the droplet generation was stable.

2.2. Printability assessments

After characterizing the droplet volumes, the printability of the developed system was analyzed. Due to its low viscosity, printing high-aspect ratio objects with fish skin-derived GelMA in the conventional setup would be generally challenging. To investigate the impact of the cryoplate on the temperature of the hydrogel, droplets were dispensed at different frequencies (20 Hz, 10 Hz, and 5 Hz) on top of each other. The cryoplate was set to either -15 °C or -5 °C. Across all experimental conditions, temperatures at the base of the printed structures closely mirrored those of the cryoplate. Notably, at -15 °C, the temperature at the top of the structures reached approximately 0 °C when employing frequencies of 20 Hz and 10 Hz, while the employment of 5 Hz resulted in temperatures of approximately -8 °C. Within the -5 °C group, the application of a

20 Hz frequency yielded positive temperatures at the top (approximately +5 °C), whereas frequencies of 10 Hz and 5 Hz displayed roughly 0 °C at the top of the structures. It is plausible that employing lower frequencies potentially allows for a more gradual freezing process of the hydrogel deposited on the top. This extended exposure to lower temperatures enables the material to adapt gradually, resulting in a slower increase in temperature as the structures freeze from their base. Afterwards, the achievable aspect ratios using our system were investigated. Droplets were dispensed with ejection frequencies between 0.1 and 20 Hz on the same spot while the cryoplate was cooled to -5, -10, or -15 °C (**Figure S1**). **Figure 2B** shows that as the frequency was decreased, the aspect ratio increased at each temperature. This was because the longer time between droplet ejection allowed the droplets to freeze on top of each other instead of merging into a larger structure with a lower aspect ratio. It is worth noting that, to the best of our knowledge, droplet-based bioprinting of such high-aspect ratio hydrogel structures using low-viscosity materials has not been demonstrated before.

At high frequencies, there were no noticeable differences observed between the temperatures. However, as the frequency was decreased, apparent differences in the aspect ratio were measured, with the lowest temperature producing the structure with the highest aspect ratio. For example, at a frequency of 20 Hz and -15 °C, a large droplet with a poor aspect ratio (<0.9) was formed, whereas a frequency of 0.1 Hz resulted in a pillar with a high aspect ratio (>4). Thus, resolution in Z-direction depends on various factors, such as the temperature of the cryoplate, the dispensing frequency, and the height of the structure. It should be noted that the maximum printable pillar height for this experiment was below 2.5 mm and further droplet deposition led to spherical structures on top of the pillars (Figure S1), limiting the printability in the Z-dimension.

Next, it was observed how the system could be used to print continuous lines. The printhead was moved with a constant speed while droplets were dispended with frequencies from 1 up to 10 Hz. A representative pattern of such prints can be seen in **Figure 2C**. These patterns were printed for three droplet volumes (0.8, 6.9, and 10.8 nL) and three different cryoplate temperatures (-5, -10, and -15 °C). As can be seen, lower frequencies resulted in singular spots, which, as frequency was increased, turned into frizzy and then smooth lines. The diameters of the printed spots/widths of the lines were measured exemplarily for the 1-, 2-, 7-, and 10-Hz groups. Results are shown in **Figure 2D-F**. Expectably, larger droplets resulted in larger diameters/widths, whereas the temperature of the cryoplate appeared to play a minor role as diameters/widths did not change for

lower temperatures. For all prints, a rate of 7 Hz with a constant printhead moving speed resulted in homogeneous lines, and this frequency/printhead moving speed ratio was chosen for future experiments. Additionally, the influence of temperature on the viscoelastic properties of the hydrogel was analyzed. Close to room temperature (18 °C), the loss modulus was higher than the storage modulus, indicating a liquid-like behavior (**Figure S2A** and **B**). [48] As the temperature was lowered, the storage modulus became larger than the loss modulus, indicating more elastic (solidlike) behavior, which may explain the structural integrity of the cryobioprinted constructs. [49] Also, at room temperature the viscosity of the used hydrogel was approximately 0.01 Pa s, which increased to over 50 Pa s after freezing (**Figure S2C**). Following the characterization of printability, sophisticated structures were printed. First, simple and complex two-dimensional (2D) geometries were deposited (Figure 2G). The approach was then utilized to print more complex supported 3D structures such as pyramids or grids, which are typically challenging to produce using dropletbased methods (Figure 2H). Finally, free-standing 3D structures, including the letters H and V in the Z-direction, among others, were created. It is worth noting that, to the best of our knowledge, such free-standing structures were, even with additional crosslinking steps, not bioprinted before using droplet-based printing/bioprinting approaches. In addition, certain features of these structures, such as the connection in the letter "H", are particularly difficult to achieve using other droplet-based or most extrusion methods. It should be noted that, printability in the X- and Ydirections is limited by the size of the cryoplate. Furthermore, the resolution in the X- and Ydirections is mainly guided by the droplet size/droplet diameter. However, resolution in the Zdirection and maximal printing height is limited by the heat-transfer kinetics with the environment.^[38,50] In the future, this drawback could be overcome by fabricating modular, assembled units.[50]

2.3. Bioprinting of C2C12 and NIH/3T3 cells

After printing complex 3D structures, it was assessed if the developed technique was suitable for cryobioprinting with embedded cells within the bioink (7.5% GelMA). First, the achievable cell viability with our in-house bioprinting system was evaluated by comparing the viability of C2C12 myoblasts bioprinted *via* microvalve (without freezing) and that of pipetted cells. Compared to pipetting, the bioprinting process decreased cell viability by 17% (**Figure S3**). This

reduction in viability fell within the range reported in previous studies utilizing microvalve bioprinting approaches.^[45]

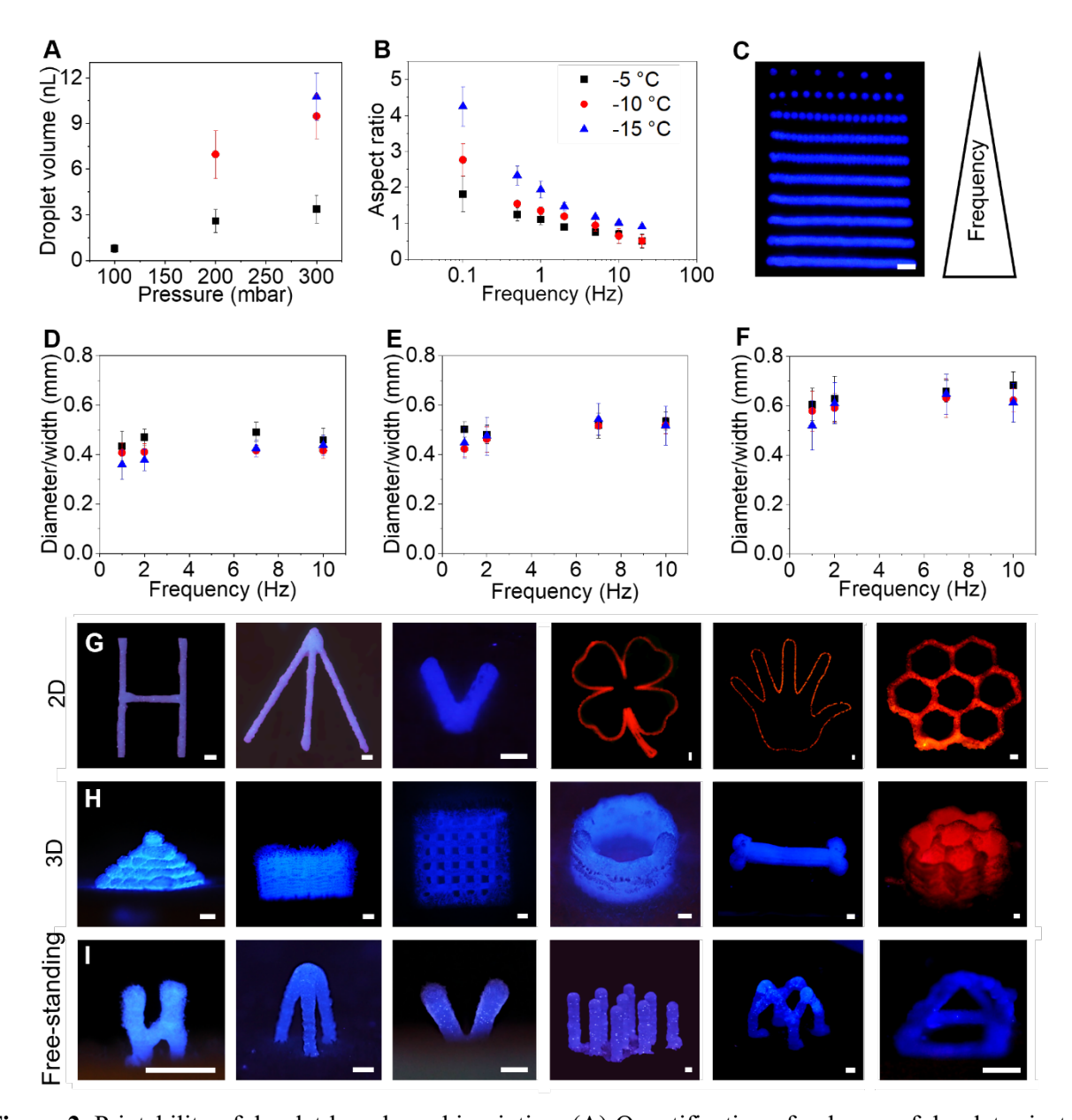


Figure 2. Printability of droplet-based cryobioprinting. (A) Quantification of volumes of droplets ejected with the microvalve for opening times of 500 (black square), 600 (red circle), and 700 μs (blue triangle) and pressures of 100, 200, and 300 mbar; n=3. (B) Quantification of aspect ratios for on-the-spot printing with different frequencies; n=5. (C) Representative pattern to characterize line printing by increasing droplet ejection frequency. (D-F) Quantifications of spot diameters or line widths for droplet sizes of (D) 0.8 nL, (E) 6.9 nL, and (F) 10.8 nL printed onto the cryoplate with temperatures of -5 (black square), -10

(red circles), and -15 °C (blue triangles); n=3. (G-I) Sophisticated 2D, 3D supported, and 3D free-standing structures printed with droplet-based cryobioprinting. Scale bars: 1 mm.

Next, the viability of C2C12 cells was evaluated by bioprinting a 4-layer grid on the cryoplate, which was cooled to -5, -10, or -15 °C. Bioprinting with temperatures of -5 and -10 °C yielded initial viabilities of approximately 50%, whereas -15 °C resulted in a low viability of only 12% (**Figure S4**), possibly due to the small droplet sizes and hence fast freezing kinetics. Therefore, only the viabilities of the -5 and -10 °C groups were evaluated for up to 14 days in culture (Figure 3A and Figure S5). Of note, the cell viabilities increased to approximately 90% at the end of the observation (Figure 3C), at which no significant difference between the viabilities of cells from both groups was measured. After viability was assessed, the samples were bioprinted onto the cryoplate at -5 and -10 °C and their morphologies were monitored over a 14-day period by performing F-actin and nuclei staining on days 3, 7, and 14 (Figure 3E, Figure S6, and Figure S7). As shown in Figure 3E, C2C12 cells were spreading at day 3 and continued to spread out in all directions during the 2-week period of culture, indicating that the cells were viable, proliferating, and forming a network of interconnected cells. In addition, the areas covered by the cells were evaluated on days 3, 7, and 14 (Figure S8). As expected, the area covered by cells increased for later days in culture. Nonetheless, the covered area was slightly, non-significantly, higher in samples that were bioprinted onto the -5 °C cryoplate compared to those that were bioprinted at -10 °C.

To further validate the presented method, we repeated the experiments with a different cell type, namely NIH/3T3 fibroblasts. Similar to C2C12 cells, bioprinting onto the cryoplate at -5 and -10 °C resulted in initial viabilities of approximately 50%, with slightly higher cell viability values observed at -5 °C. Bioprinting onto the cryoplate at -15 °C resulted in a low viability of only 20% (**Figure S9**), and this group was not evaluated further. The viabilities of samples bioprinted onto the cryoplate at -5 and -10 °C were monitored for 2 weeks (**Figure 3B**, **Figure 3D**, and **Figure S10**), which reached a significant difference of approximately 80% and 67%, respectively. The slight differences in viabilities between C2C12 and NIH/3T3 cells might be attributed to the varying effects of freezing on different cell types. Moreover, cell viability can also be influenced by different factors such as cell batch, passage, and experimental conditions. Despite the initial viability of 50%, the increase of up to 80% suggested that the droplet-based cryobioprinting

method was appropriate for cell-laden bioprinting applications. Moreover, the spreading of NIH/3T3 cells on day 3 and the continued growth over the 14-day culture period, as shown in **Figure 3F**, **Figure S11**, and **Figure S12**, further supported feasibility of the approach for bioprinting cells. Again, the area covered by cells increased with the number of days, and the samples bioprinted onto the cryoplate at -5 °C displayed the highest amount of cellular area coverage (**Figure S13**).

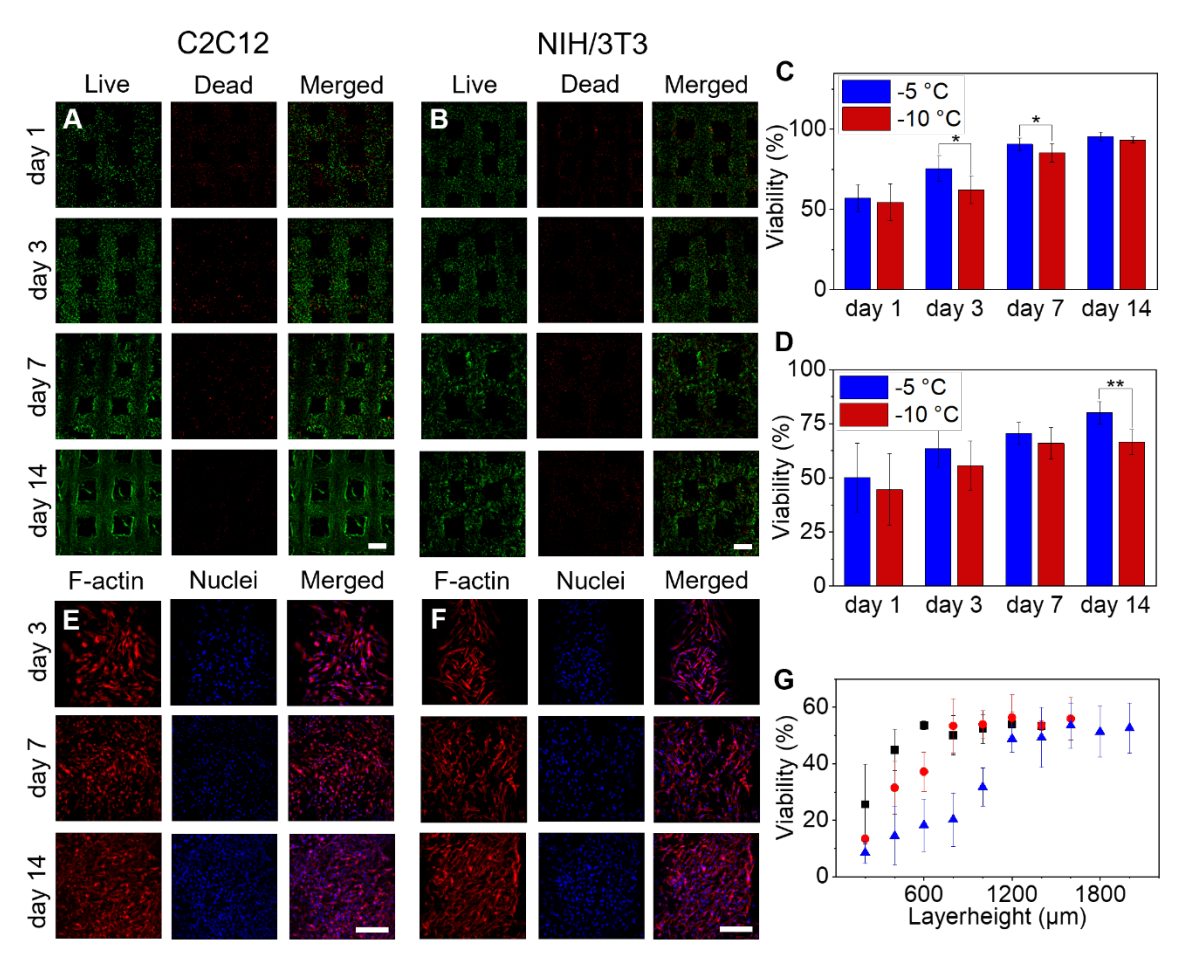


Figure 3. Bioprinting of C2C12 and NIH/3T3 cells via droplet-based cryobioprinting. (A, B) Representative fluorescence live (green) and dead (red) images of printed grids containing C212 and NIH/3T3 cells, respectively, on days 1, 3, 7, and 14. Scale bars: 500 μm. (C, D) Quantification of viability of C2C12 and NIH/3T3 cells, respectively, over 14 days of incubation; *p < 0.05, **p < 0.001; n=3. (E, F) Representative fluorescence images of F-actin (red) and cell nuclei (blue) stained C2C12 and NIH/3T3 cells at days 3, 7, and 14 of incubation. Scale bars: 200 μm. (G) Segmented quantification of viability of C2C12 cells bioprinted as pillars onto the cryoplate cooled to -5 °C (black square), -10 °C (red circle), and -15 °C (blue triangle); n=3.

2.4. Influence of layer height and temperature on viability

Due to the major differences observed in viabilities for C2C12 and NIH/3T3 cells between the -5/-10 °C and the -15 °C group, and to gain a better understanding of the influence of the freezing behavior on the viability of the cells, C2C12 were bioprinted as vertical pillars on the cryoplate that was cooled to -5, -10, or -15 °C. The pillars were divided into 200-μm segments, and cell viability was analyzed within each segment (**Figure 3G** and **Figure S14**) on the first day post-bioprinting. For each temperature, the first segment (closest to the plate) had the lowest cell viability at approximately 25% for -5 °C, approximately 13% for -10 °C, and approximately 8% for -15 °C. This increase in cell death might be explained by the negative influence of higher cooling rates on cell viability, [51,52] which were the highest in the layers closest to the cryoplate.

As revealed, viability increased for higher layers and viabilities of approximately 50% were reached at 600 μm in the -5 °C, at 800 μm in the -10 °C, and at 1,200 μm in the -15 °C groups. It should be noted that, as discussed earlier, -5 °C yielded lower pillars than -15 °C, which is why no viability data is presented after a layer height of 1,200 μm. Similarly, no viability data could be obtained for -10 °C after a layer height of 1,600 μm.

Due to the negative impact of the substrate temperature and based on the previous results, all following experiments were conducted with a cryoplate temperature of -5 °C. It should be mentioned that for our previous work based on extrusion-based cryobioprinting, [39,40] lower temperatures were used for bioprinting, which had a less negative impact on cell viability compared to droplet-based cryobioprinting. The observed variations might be attributed to differences in the employed bioprinting modalities. Specifically, the droplet-based method involved the utilization of relatively small droplets that were ejected at room temperature and promptly frozen upon contact with the cryoplate. In contrast, the extrusion-based approach entailed the deposition of broader filaments and the continuous extrusion of hydrogel, potentially introducing dissimilarities in the freezing mechanism, which requires further in-depth analyses in the future, which however, is out of scope of the current work. Nonetheless, future work could focus on developing a printing system with integrated cooling control instead of rapid freezing of the bioink, which may enable to further decrease the thermal stress on cells.

2.5. Bioprinting of astrocytes with different GelMA concentrations

Astrocytes are the most abundant cell type in the brain and play a crucial role within the central nervous system, for example, in synaptic transmission or information processing.^[53,54] It is known that their functions and organizations heavily depend on interactions with the ECM and its stiffness.^[54,55] To preliminarily investigate if the presented droplet-based cryobioprinting approach could be beneficial for reproducing astrocyte behaviors in vitro, they were thus bioprinted embedded in 3% GelMA (hydrogel-precursors with lower concentrations could not be crosslinked) and 7.5% GelMA (**Figure 4A**) as four-layer grids onto the cryoplate, that was set to -5 °C, with a concentration of 5×10⁶ cells mL⁻¹.

Initially, cell viability values were approximately 50% on day 1 for both groups (Figure 4B-**D**), which was in the range of viabilities of C2C12 and NIH/3T3 cells discussed above. However, on day 7, a significant difference between viabilities in the 3% group (approximately 80%) and the 7.5% group (~60%) was observed, which was still observable on day 14 (approximately 90% and 70%, respectively). Moreover, their organizations were analyzed via F-actin and nucleus staining (Figure 4E and F). Despite bioprinting the same cell density in both groups, astrocytes in the 3% GelMA covered significantly more areas already on day 3 post-bioprinting compared to the 7.5% group (Figure 4G). While the covered area in the 3% group almost three-folded after 14 days, the area covered by cells only increased marginally in the 7.5% group. It has been previously reported that astrocytes spread less in stiffer extracellular matrix biomaterials, which may explain these observations.^[55] Hence, these findings indicated the feasibility of customizing the hydrogel to meet the specific needs of desired cell types, thereby facilitating the creation of a favorable microenvironment for cells that prefer soft 3D environmental conditions fabricated via dropletbased cryobioprinting otherwise not attainable without the use of the cryoplate. It should be mentioned that, despite favorable behaviors of astrocytes in the 3% group, the bioprinted structures displayed less stable shape fidelity during the 2-week culture, which was most likely caused by the low GelMA concentration. Therefore, future research should address how droplet-based cryobioprinting may be utilized to bioprint tissue constructs with very low polymer concentrations and how to improve their long-term stability.

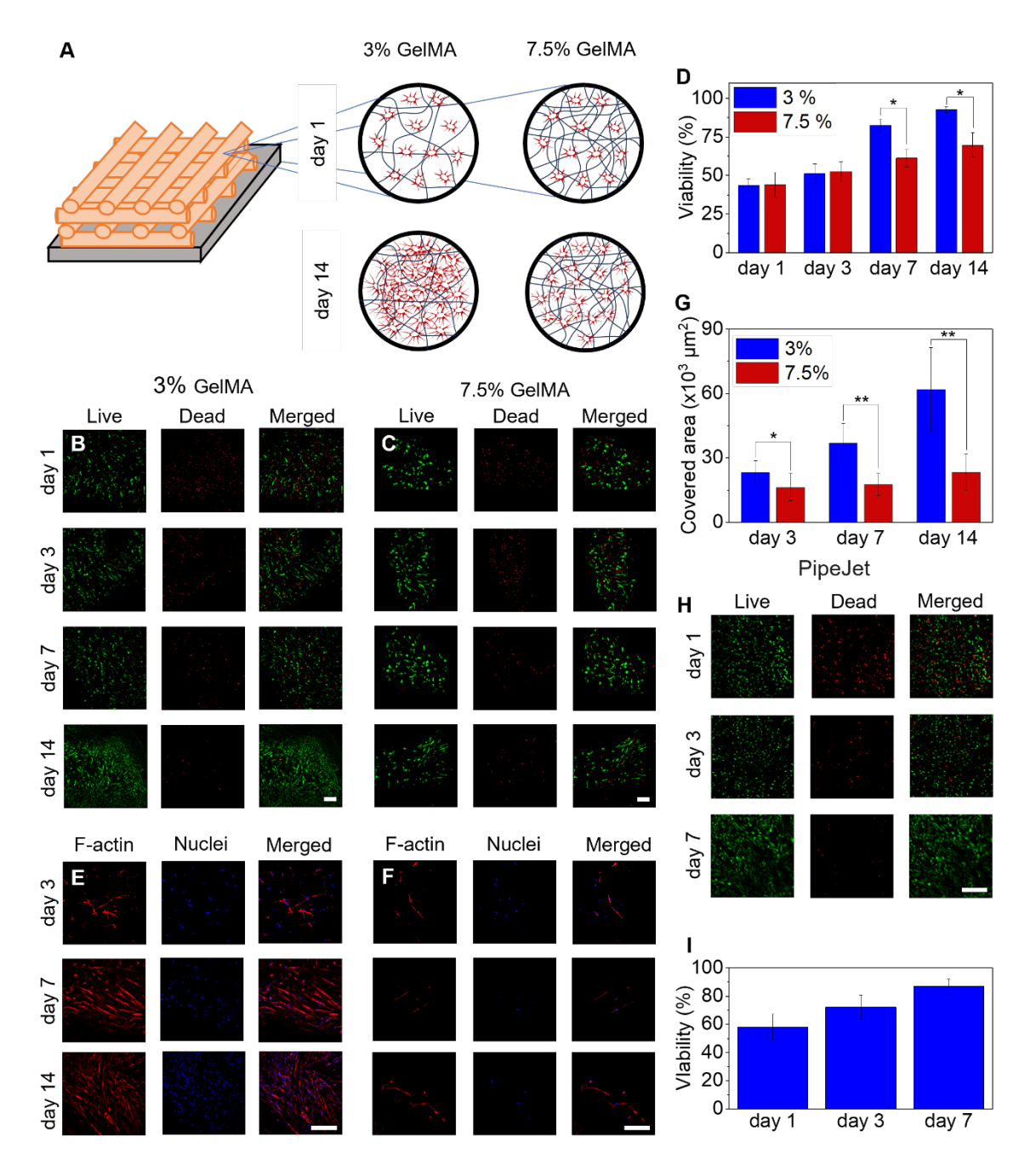


Figure 4. Droplet-based cryobioprinting with different GelMA concentrations and higher cell densities. (A) Schematic illustration of droplet-based cryobioprinting of astrocytes encapsulated in 3% and 7.5% GelMA. (B, C) Representative fluorescence live (green) and dead (red) images of astrocytes in 3% and 7.5% GelMA on days 1, 3, 7, and 14. (D) Quantification of viability of astrocytes in both GelMA concentrations over 14 days of culture; n=3. (E, F) Representative fluorescence images of F-actin (red) and cell nuclei (blue) of astrocytes in 3% and 7.5% GelMA on days 3, 7, and 14 of incubation. (G) Quantification of the area covered by astrocytes in 3% and 7.5% GelMA; n=3. (H) Representative

fluorescence live (green) and dead (red) images of HUVECs bioprinted at higher cell densities. (I) Quantification of HUVEC viabilities on days 1, 3, and 7; n=3. Scale bars: 200 μ m; *p < 0.05, **p < 0.001.

2.6. Droplet-based cryobioprinting with high cell density

Usually, microvalve-based bioprinting is limited to bioinks with cell densities in the 10⁶-cells mL⁻¹ range,^[45] which is roughly two or three orders of magnitude lower than human tissue (approximately 1-3 billion cells mL⁻¹).^[56,57] Therefore, we evaluated whether the developed approach could be utilized to bioprint with higher cell densities. Hence, for this experiment, the microvalve was exchanged for a piezoelectric drop-on-demand (DoD) dispenser that has been previously applied to bioprint high cell densities and functional structures.^[20,21,25,58]. Since vasculature is one of the cornerstones for producing viable and functional tissues, a bioink containing human umbilical vein endothelial cells (HUVECs), with a density of 2.5×10⁷ cells mL⁻¹, was prepared, and a four-layer grid was bioprinted onto the cryoplate. On day 1, approximately 60% of cells were alive, and subsequently, viability increased to approximately 90% during 7 days of incubation (**Figure 4H and I**). These results indicated that droplet-based cryobioprinting was not limited to microvalves and highlighted that it may also be applied to other droplet-based bioprinting techniques to facilitate improved biological relevancy.

2.7. Multi-material droplet-based cryobioprinting

In most tissues, multiple types of cells are arranged in 3D structures that enable them to communicate and perform their respective functions. However, as discussed, patterning 3D structures using droplet-based bioprinting techniques can be challenging. Although laser-assisted bioprinting has demonstrated the ability to fabricate 3D structures, [7,59] it is, especially when printing multiple materials, a time-consuming fabrication method.[29,30] Microvalve and inkjet approaches, on the other hand, typically necessitate a crosslinking step after each layer to address droplet wetting and spreading issues. This requirement adds complexity and difficulty to the process of producing complex, multi-material 3D structures.[7,31,32] For example, previously, droplet-based bioprinting of patterned 3D constructs was achieved by bioprinting aqueous droplets into an oil bath, followed by a waiting period at 4 °C for gelation, removal of lipids in the oil, coating with a layer of cell-free ink, a second waiting period, and finally transfer to the culture medium.^[7]

Droplet-based cryobioprinting that we report in this work addresses several of these hurdles. Due to the rapid freezing of the bioink, it is possible to bioprint complex architectures consisting of various materials without any additional steps besides bioprinting and crosslinking post-bioprinting. These architectures display spatial heterogeneity of different materials without uncontrolled mixing. To demonstrate the proof-of-concept multi-material potential of our approach, two valves were filled with 7.5% GelMA, in this case containing no cells but mixed with aqueous fluorescent dyes of different colors. **Figure 5A** shows a collection of printed 2D patterns.

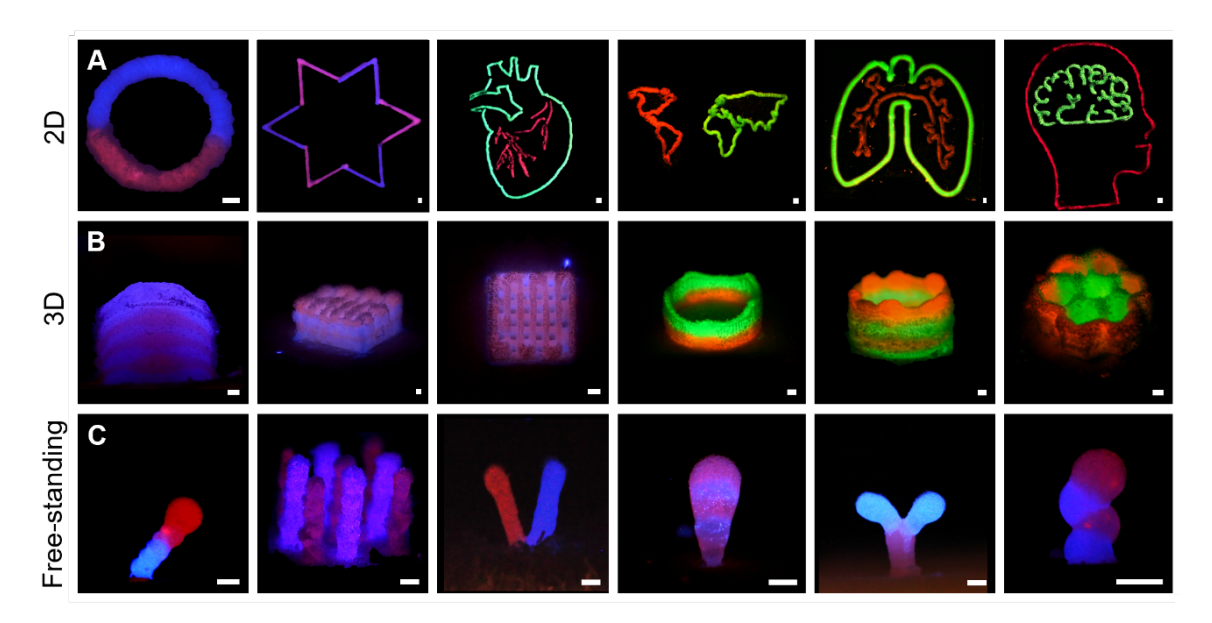


Figure 5. Multi-material structures printed *via* droplet-based cryobioprinting. (A-C) Sophisticated 2D, 3D supported, and 3D free-standing structures containing two materials printed with droplet-based cryobioprinting. Scale bars: 1 mm.

In **Figure 5B**, 3D constructs, for example, a grid with alternating materials between layers, are shown, demonstrating that this approach is suitable for fabricating complex volumetric structures consisting of various materials. It should be mentioned that the number of valves in the system was the only limiting factor for the number of materials. Future experiments could be conducted with more materials by including more valves, paving the way to print even more sophisticated patterns. Perhaps, most importantly, **Figure 5C** displays how the droplet-based cryobioprinting method can be applied to print free-standing, self-supporting structures consisting of multiple materials without additional support structures or scaffolds. This enables to print complex

structures, including overhanging structures, which again, to our knowledge, has yet not been demonstrated for droplet-based bioprinting approaches. Overall, these results illustrate how the presented method can be used to produce complex, 3D objects with precise control over the placement of different cells and bioink. It is of note that the inks did not noticeably mix in areas where they overlapped, due to their frozen state, whereas they would otherwise mix uncontrollably without the cryoplate. This characteristic allowed for more precise placement of droplets to achieve physiologically relevant cell-laden tissue bioprinting in the future.

2.8. Droplet-based cryobioprinting of endothelialized breast cancer model

It is challenging to fabricate the spatial heterogeneity of mammalian tissues via bioprinting of low-viscosity materials due to uncontrolled mixing of the bioinks. [60] To demonstrate that the presented approach can overcome this shortcoming, a vascularized breast tumor model was fabricated as proof of concept of multi-material droplet-based cryobioprinting. Before bioprinting the co-culture of both cell types, the individual viabilities of both cell types in endothelial cell culture medium were evaluated when bioprinted via droplet-based cryobioprinting. While initial cell viabilities were again low for both cell types, the viabilities increased to decent values over 21 days of culture and reached approximately 90% and 80% for HUVECs and MCF-7 cells, respectively (compare Figures S15-S18). Next, the co-culture model was fabricated by first bioprinting two layers of MCF-7 cells with a concentration of 2.5×10⁶ cells mL⁻¹. Subsequently, two layers of (green fluorescent protein, GFP)-HUVECs, with a concentration of 5×10⁶ cells mL⁻ ¹, were bioprinted in the shape of a vasculature, on top of the MCF-7 cells. Afterwards, the samples were cultured for up to 21 days (see **Figure 6A**). It can be observed that the two cell types did not mix, which they would without the cryoplate, and that the HUVEC structure was intact during the entire incubation period. Moreover, it is visible that endothelial cells and tumor cells proliferated during the 21-day period. However, at the intersection of both cell types (Figure 6B), it appears that trace outward sprouting of endothelial cells towards the MCF-7 cells was visible. This is most likely caused by the given height difference between the cell types, since HUVECs were bioprinted on top of the MCF-7 cells. Thus, HUVECs are not entirely surrounded by MF7-cells. Nonetheless, these preliminary experiments demonstrated that droplet-based cryobioprinting can be applied to precisely structure constructs with multiple cell populations in a straight-forward manner.

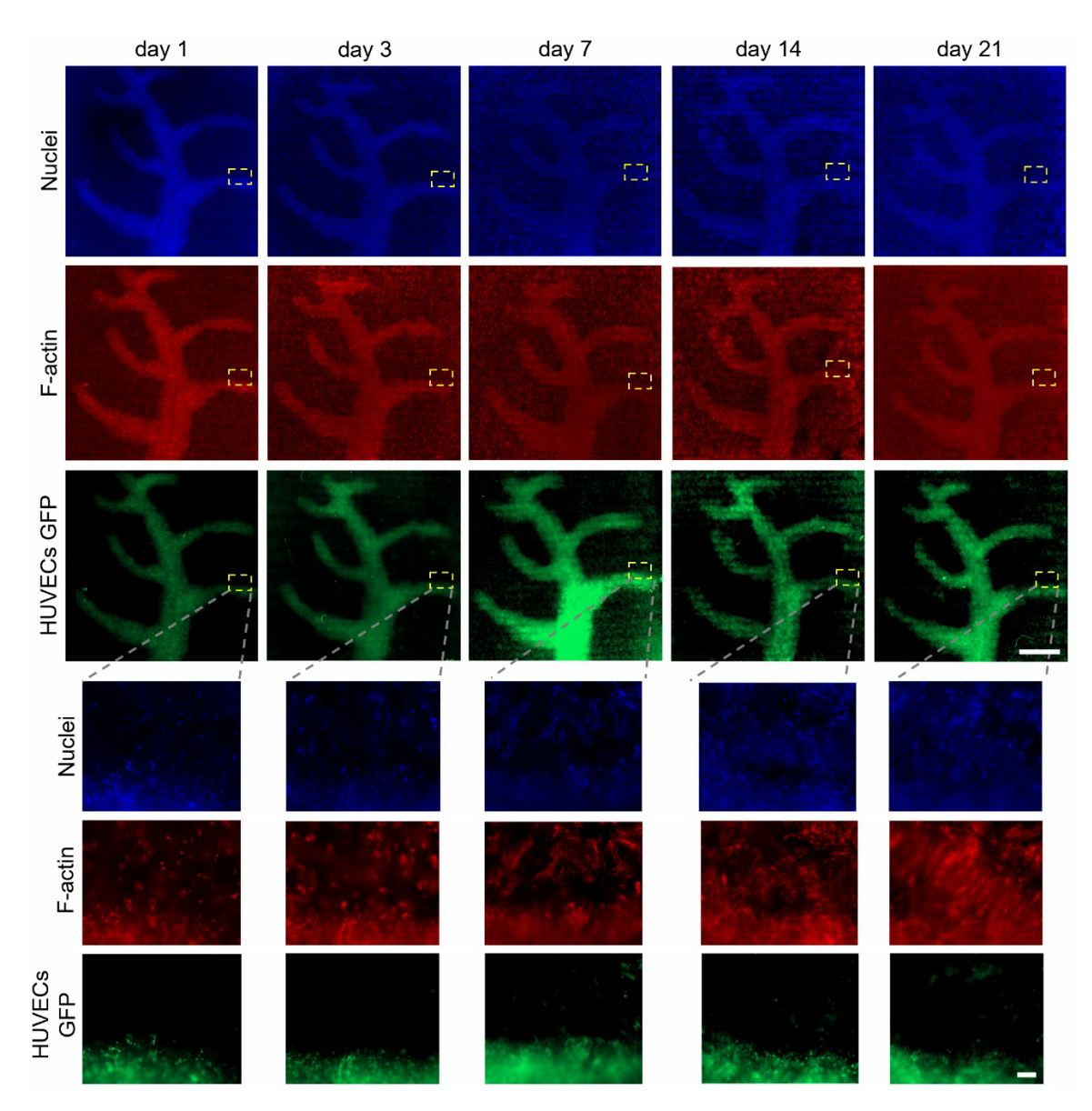


Figure 6. Endothelialized breast-cancer model fabricated via droplet-based cryobioprinting. (A) Representative fluorescent images of the cell nuclei (blue), F-actin (red) and GFP-HUVECs (green) of the entire bioprinted construct on days 1, 3, 7, 14, 21. Scale bar: 2 mm. (B) Representative fluorescence images at the intersection of MCF-7 cells and HUVECs on days 1, 3, 7, 14, 21. Scale bar: 100 μm.

3 Conclusions

Droplet-based bioprinting has emerged as an attractive technique for bioprinting in recent years. Nevertheless, due to the necessary low viscosity values of the used bioinks, it is oftentimes complicated and labor-intensive to fabricate complex 3D geometries and to spatially pattern such constructs with different materials. In this study, we introduced a cryobioprinting technique

merging droplet-based and cryogenic bioprinting. The printing system reliably generated droplets in the range of 1-10 nL. By maintaining the low-viscosity bioink at ambient temperature, it stayed liquid throughout the printing procedure, ensuring consistent droplet formation. It was presented how this approach could be utilized to fabricate sophisticated volumetric objects, including self-supporting structures, via a simple process (bioprinting, and crosslinking only after the entire bioprinting process) with no additional steps. Moreover, we bioprinted structures using cryoprotective bioinks laden with different cell types to demonstrate how this approach could be utilized for bioprinting. With our proof-of-concept demonstrations, it is anticipated that our droplet-based cryobioprinting method complements current droplet-based bioprinting techniques and paves new avenues for these methods to fabricate physiologically and biologically relevant volumetric and multi-cell-type tissue constructs.

4 Experimental Section

4.1. GelMA synthesis

Unless declared otherwise, all materials were purchased from Sigma-Aldrich, and GelMA was synthesized according to a previously published protocol. [12,42,61] In short, first, gelatin derived from fish skin was dissolved in phosphate-buffered saline (PBS, ThermoFisher Scientific) at a concentration of 10% (w/v) at 50 °C. Then, over 1 hour, methacrylic anhydride was slowly added using a syringe pump until a concentration of 8% (v/v) was reached. The emulsion was thoroughly mixed on a magnetic hot plate for 3 hours at 50 °C to ensure homogeneity. The resulting solution was diluted once with PBS and dialyzed with distilled water for 1 week at 40 °C, with the distilled water changed every 12 hours. Subsequently, the solution was filtered at 40 °C using a 0.22-µm Stericup-GP Sterile Vacuum Filtration System (Millipore) and then aliquoted into 40 mL portions and stored at -80 °C for at least 24 hours. Afterwards, the frozen GelMA was lyophilized for 5 days at 0.2 mbar and 24 °C in a FreeZone Labconco freeze-dryer.

4.2. Cell Culture

Five different cell types were used: mouse C2C12 skeletal myoblasts, mouse NIH/3T3 fibroblasts, human astrocytes, HUVECs, and human MCF-7 breast cancer cells. All, except astrocytes and HUVECs, were cultured in Dulbecco's modified Eagle's medium (DMEM, Thermo Fisher Scientific) that was supplemented with 10% (v/v) FBS (Thermo Fisher Scientific) and 1%

(v/v) antibiotic-antimycotic (AA, Thermo Fisher Scientific). Astrocytes were cultured in DMEM that was supplemented with 10% (v/v) FBS and 1% (v/v) AA, 1% sodium pyruvate (v/v), and 2% glutamax (v/v). Based on previous reports, [62–64] HUVECs, MCF-7 cells (after printing) and HUVEC/MCF-7 co-culture were cultured in endothelial cell culture medium (EBM-2, Lonza Biologics) that was supplemented with the endothelial growth BulletKit and 1% AA. The cells were cultured in T75 or T175 flasks in an incubator with 37 °C and 5% CO₂. Culture media were changed every second day until cells were approximately 80% confluent, after which they were either passaged or harvested for bioprinting.

4.3. Bioink preparation

GelMA with a final concentration of 7.5% (w/v) was used for all experiments unless stated otherwise. It was dissolved in a solution with 80% PBS (v/v), 10% FBS (v/v), and 10% DMSO (v/v). In addition, 0.3% (w/v) lithium phenyl-2,4,6-trimethylbenzoylphosphinate (LAP, Advanced Biomatrix) and 8% D-(+)-melezitose hydrate (w/v) (Alfa Aesar) were added to formulate the bioink. After dissolving all components, the bioink was sterilized *via* a heating-cooling cycle in which it was alternatingly stored in an 80 °C oven for 10 minutes and then in a 4 °C fridge for 15 minutes. This step was repeated three consecutive times. Unless mentioned otherwise, before bioprinting, cells were harvested and mixed with the bioink to obtain a concentration of 5×106 cells mL⁻¹ for use with the microvalve or 2.5×10⁷ cells mL⁻¹ for the PipeJet system.

4.4. Droplet-based cryobioprinting

A commercially available microvalve (Fritz Gyger AG) was mounted onto an in-house bioprinting system. Repetier-Host (Hot-World GmbH & Co. KG) was used to control the bioprinter and load the corresponding G-codes. The reservoirs of the microvalves were connected to an in-house pressure-regulator, which could apply pressures between 0 and 400 mbar in 1-mbar steps. Before each print, the microvalve was rinsed with ethanol for sterilization and, subsequently, with sterile PBS. Afterwards, the bioink was transferred into the reservoir of the microvalve. Alternatively, the microvalve was exchanged with a DoD dispenser (PipeJet nanodispenser, prior described in, [65] BioFluidix GmbH). The bioink in the microvalve was kept at room temperature. A custom-build cryoplate that was used for extrusion-based cryobioprinting, [39,40] which was set between -5 °C and -15 °C, was used as a bioprinting substrate. Directly after bioprinting, the

constructs on the cryoplate were crosslinked under UV irradiation for 30 seconds and afterward the cryoplate was turned off. If cells were used, the constructs were transferred into the corresponding prewarmed (37 °C) cell culture medium to ensure rapid rewarming of the cells, which has been shown to be beneficial for cell viability when thawing.^[66] Finally, if cells were used, the bioprinted constructs were incubated in the corresponding cell culture medium that was refreshed every other day.

4.5. Live/dead assay

To evaluate the viability of cells, a live/dead assay was performed on days 1, 3, 7, and 14 post-bioprinting. The assay was prepared by dissolving 1 μ L mL⁻¹ of calcein-AM (Thermo Fisher Scientific) and 2 μ L mL⁻¹ of ethidium-homodimer-1 (Thermo Fisher Scientific) in PBS. The samples were immersed in the staining solution and incubated for 30 minutes in the dark. Afterwards, cells were washed twice with PBS and imaged with an inverted Eclipse-Ti fluorescence microscope (Nikon). Live and dead cells were counted manually or via the ImageJ software (National Institutes of Health), and viability was quantified by dividing the number of live cells over the number of total cells. Per sample, images of at least three different regions were taken and n=3 samples were analyzed per condition.

4.6. Immunostaining and cell coverage analyses

Bioprinted samples were fixed on days 3, 7, and 14 with 10% (v/v) paraformaldehyde for 15 minutes at room temperature. A staining solution was prepared by dissolving 5 μL mL⁻¹ of AlexaFluor 594-labeled F-actin (Thermo Fisher Scientific) in a blocking buffer in which the samples were incubated at 4 °C under gentle shaking overnight. Next, the staining solution was removed, and the samples were incubated in a 4',6-diamidino-2-phenylindole (DAPI) (Vector Laboratories) solution (100 nmol L⁻¹) solution for 15 minutes at room temperatures, and then the samples were washed two times. Finally, images were obtained with the fluorescent microscope. To evaluate the areas covered by cells within constructs, images of F-actin-stained cells were taken. If not stated otherwise, n=3 samples were used for analysis. These images were then analyzed via the particle analysis of the ImageJ software and the areas covered by cells were obtained.

4.7. Droplet size measurement

An optical system (SmartDrop, BioFuidix GmbH,) was used to analyze and record the shapes of the dispended droplets in flight. The system captures an image of the droplet in-flight after ejection, and, based on the shape of the droplet, the volume of each individual droplet can be calculated. A total of n=3 runs were performed, with at least n=1,000 droplets measured per each run and parameter.

4.8. Statistical Analysis

To compare results from two different groups, statistical significances were analyzed *via* a two-sample t-test. A probability value of *p<0.05 indicated statistical significance, with increasing significances for **p<0.001.

Data availability statement

All data needed to evaluate the conclusions in the paper are present in the paper and/or the Supplementary Materials. Additional data related to this paper may be requested from the authors.

Acknowledgements

The authors acknowledge the support from the National Institutes of Technology (R01HL153857, R01HL166522, R56EB034702, R01CA282451), National Science Foundation (CBET-EBMS-1936105, CISE-IIS-2225698), Chan Zuckerberg Initiative (2022-316712), and the Brigham Research Institute.

Declaration of competing interest

YSZ consulted for Allevi by 3D Systems, and sits on the scientific advisory board and holds options of Xellar, neither of which however, participated in or bias the work. The other authors declare that they have no known competing financial interests or personal relationships that could have appeared to influence the work reported in this paper.

References

- [1] S. v Murphy, A. Atala, *Nat Biotechnol* **2014**, *32*, 773.
- [2] F. Koch, K. Tröndle, G. Finkenzeller, R. Zengerle, S. Zimmermann, P. Koltay, *Bioprinting* **2020**, *20*, e00094.

- [3] S. Ramesh, O. L. A. Harrysson, P. K. Rao, A. Tamayol, D. R. Cormier, Y. Zhang, I. v. Rivero, *Bioprinting* **2021**, *21*, e00116.
- [4] Y. S. Zhang, G. Haghiashtiani, T. Hübscher, D. J. Kelly, J. M. Lee, M. Lutolf, M. C. McAlpine, W. Y. Yeong, M. Zenobi-Wong, J. Malda, *Nature Reviews Methods Primers* **2021**, *1*, 75.
- [5] T. Jiang, J. G. Munguia-Lopez, S. Flores-Torres, J. Kort-Mascort, J. M. Kinsella, *Appl Phys Rev* **2019**, *6*, 011310.
- [6] C. Mazzaglia, Y. Sheng, L. N. Rodrigues, I. M. Lei, J. D. Shields, Y. Y. S. Huang, *Biofabrication* **2023**, *15*, 025005.
- [7] A. D. Graham, S. N. Olof, M. J. Burke, J. P. K. Armstrong, E. A. Mikhailova, J. G. Nicholson, S. J. Box, F. G. Szele, A. W. Perriman, H. Bayley, *Sci Rep* **2017**, *7*, 7004.
- [8] H. Gudapati, M. Dey, I. Ozbolat, Biomaterials 2016, 102, 20.
- [9] C. Xu, M. Zhang, Y. Huang, A. Ogale, J. Fu, R. R. Markwald, *Langmuir* **2014**, *30*, 9130.
- [10] R. Levato, O. Dudaryeva, C. E. Garciamendez-Mijares, B. E. Kirkpatrick, R. Rizzo, J. Schimelman, K. S. Anseth, S. Chen, M. Zenobi-Wong, Y. S. Zhang, *Nature Reviews Methods Primers* **2023**, *3*, 47.
- [11] S. H. Kim, D. Y. Kim, T. H. Lim, C. H. Park, **2020**, pp. 53–66.
- [12] M. Wang, W. Li, L. S. Mille, T. Ching, Z. Luo, G. Tang, C. E. Garciamendez, A. Lesha, M. Hashimoto, Y. S. Zhang, *Advanced Materials* **2022**, *34*, 2107038.
- [13] Y. Lu, G. Mapili, G. Suhali, S. Chen, K. Roy, *J Biomed Mater Res A* **2006**, 77A, 396.
- [14] D. Kilian, T. Ahlfeld, A. R. Akkineni, A. Lode, M. Gelinsky, MRS Bull 2017, 42, 585.
- [15] J. Gehlen, W. Qiu, G. N. Schädli, R. Müller, X.-H. Qin, Acta Biomater 2023, 156, 49.
- [16] P. N. Bernal, M. Bouwmeester, J. Madrid-Wolff, M. Falandt, S. Florczak, N. G. Rodriguez, Y. Li, G. Größbacher, R. Samsom, M. van Wolferen, L. J. W. van der Laan, P. Delrot, D. Loterie, J. Malda, C. Moser, B. Spee, R. Levato, *Advanced Materials* **2022**, *34*, 2110054.
- [17] M. Xie, L. Lian, X. Mu, Z. Luo, C. E. Garciamendez-Mijares, Z. Zhang, A. López, J. Manríquez, X. Kuang, J. Wu, J. K. Sahoo, F. Z. González, G. Li, G. Tang, S. Maharjan, J. Guo, D. L. Kaplan, Y. S. Zhang, *Nat Commun* **2023**, *14*, 210.
- [18] X. Li, B. Liu, B. Pei, J. Chen, D. Zhou, J. Peng, X. Zhang, W. Jia, T. Xu, *Chem Rev* **2020**, *120*, 10793.
- [19] A. Yusof, H. Keegan, C. D. Spillane, O. M. Sheils, C. M. Martin, J. J. O'Leary, R. Zengerle, P. Koltay, *Lab Chip* **2011**, *11*, 2447.
- [20] J. Weygant, F. Koch, K. Adam, K. Tröndle, R. Zengerle, G. Finkenzeller, S. Kartmann, P. Koltay, S. Zimmermann, *Cells* **2023**, *12*, 646.
- [21] K. Tröndle, L. Rizzo, R. Pichler, F. Koch, A. Itani, R. Zengerle, S. S. Lienkamp, P. Koltay, S. Zimmermann, *Biofabrication* **2021**, *13*, 035019.
- [22] T. Xu, W. Zhao, J.-M. Zhu, M. Z. Albanna, J. J. Yoo, A. Atala, *Biomaterials* **2013**, *34*, 130.
- [23] T. XU, C. GREGORY, P. MOLNAR, X. CUI, S. JALOTA, S. BHADURI, T. BOLAND, *Biomaterials* **2006**, DOI 10.1016/j.biomaterials.2006.01.048.
- [24] X. Cui, T. Boland, *Biomaterials* **2009**, *30*, 6221.
- [25] K. Tröndle, F. Koch, G. Finkenzeller, G. B. Stark, R. Zengerle, P. Koltay, S. Zimmermann, J Tissue Eng Regen Med 2019, 13, 1883.
- [26] P. Calvert, *Chemistry of Materials* **2001**, *13*, 3299.
- [27] A. B. Dababneh, I. T. Ozbolat, J Manuf Sci Eng 2014, 136, DOI 10.1115/1.4028512.
- [28] S. Ji, M. Guvendiren, APL Bioeng **2021**, *5*, 011508.
- [29] Z. Gu, J. Fu, H. Lin, Y. He, *Asian J Pharm Sci* **2020**, *15*, 529.

- [30] S. V Murphy, A. Atala, *Nat Biotechnol* **2014**, *32*, 773.
- [31] C. Li, A. Faulkner-Jones, A. R. Dun, J. Jin, P. Chen, Y. Xing, Z. Yang, Z. Li, W. Shu, D. Liu, R. R. Duncan, *Angewandte Chemie International Edition* **2015**, *54*, 3957.
- [32] U. A. Gurkan, R. El Assal, S. E. Yildiz, Y. Sung, A. J. Trachtenberg, W. P. Kuo, U. Demirci, *Mol Pharm* **2014**, *11*, 2151.
- [33] M. Y. Teo, S. Kee, N. RaviChandran, L. Stuart, K. C. Aw, J. Stringer, ACS Appl Mater Interfaces 2020, 12, 1832.
- [34] K. Christensen, A. Compaan, W. Chai, G. Xia, Y. Huang, ACS Biomater Sci Eng 2017, 3, 3687.
- [35] A. M. Compaan, K. Christensen, Y. Huang, ACS Biomater Sci Eng 2017, 3, 1519.
- [36] K. Christensen, C. Xu, W. Chai, Z. Zhang, J. Fu, Y. Huang, *Biotechnol Bioeng* **2015**, *112*, 1047.
- [37] A. Garg, S. S. Yerneni, P. Campbell, P. R. LeDuc, O. B. Ozdoganlar, *Advanced Science* **2022**, *9*, 2201566.
- [38] F. Zheng, Z. Wang, J. Huang, Z. Li, *Microsyst Nanoeng* **2020**, *6*, 89.
- [39] Z. Luo, G. Tang, H. Ravanbakhsh, W. Li, M. Wang, X. Kuang, C. E. Garciamendez-Mijares, L. Lian, S. Yi, J. Liao, M. Xie, J. Guo, Z. Zhou, Y. S. Zhang, *Advanced Materials* **2022**, *34*, 2108931.
- [40] H. Ravanbakhsh, Z. Luo, X. Zhang, S. Maharjan, H. S. Mirkarimi, G. Tang, C. Chávez-Madero, L. Mongeau, Y. S. Zhang, *Matter* **2022**, *5*, 573.
- [41] H. J. Yoon, S. R. Shin, J. M. Cha, S.-H. Lee, J.-H. Kim, J. T. Do, H. Song, H. Bae, *PLoS One* **2016**, *11*, e0163902.
- [42] Q. Liu, L. S. Mille, C. Villalobos, I. Anaya, M. Vostatek, S. Yi, W. Li, J. Liao, H. Wu, Y. Song, L. Xiong, Y. S. Zhang, *Biodes Manuf* **2023**, *6*, 373.
- [43] M. B. Aljaber, F. Verisqa, Z. Keskin-Erdogan, K. D. Patel, D. Y. S. Chau, J. C. Knowles, *Biomolecules* **2023**, *13*, DOI 10.3390/biom13050811.
- [44] S. Park, D. R. Lee, J. S. Nam, C. W. Ahn, H. Kim, *Cryobiology* **2018**, *81*, 65.
- [45] W. L. Ng, J. M. Lee, W. Y. Yeong, M. Win Naing, *Biomater Sci* **2017**, *5*, 632.
- [46] L. Wang, W. Kong, P. Bian, F. Wang, H. Liu, AIP Adv 2022, 12, 095310.
- [47] J. Sun, J. H. Ng, Y. H. Fuh, Y. S. Wong, H. T. Loh, Q. Xu, *Microsystem Technologies* **2009**, *15*, 1437.
- [48] H. Herrada-Manchón, M. A. Fernández, E. Aguilar, Gels 2023, 9, 517.
- [49] S. Gu, G. Cheng, T. Yang, X. Ren, G. Gao, *Macromol Mater Eng* **2017**, *302*, DOI 10.1002/mame.201700402.
- [50] Z. Luo, L. Lian, T. Stocco, J. Guo, X. Mei, L. Cai, S. M. Andrabi, Y. Su, G. Tang, H. Ravanbakhsh, W. Li, M. Wang, X. Kuang, C. E. Garciamendez-Mijares, D. Wang, Z. Wang, J. Liao, M. Xie, J. Xie, H. Kang, A. O. Lobo, Z. Zhou, Y. S. Zhang, *Adv Funct Mater* 2024, 34, DOI 10.1002/adfm.202309173.
- [51] F. Dumont, P.-A. Marechal, P. Gervais, Appl Environ Microbiol 2006, 72, 1330.
- [52] J. Baboo, P. Kilbride, M. Delahaye, S. Milne, F. Fonseca, M. Blanco, J. Meneghel, A. Nancekievill, N. Gaddum, G. J. Morris, *Sci Rep* **2019**, *9*, 3417.
- [53] M. V. Sofroniew, H. V. Vinters, *Acta Neuropathol* **2010**, *119*, 7.
- [54] I. Matthiesen, M. Jury, F. Rasti Boroojeni, S. L. Ludwig, M. Holzreuter, S. Buchmann, A. Åman Träger, R. Selegård, T. E. Winkler, D. Aili, A. Herland, *Sci Technol Adv Mater* 2023, 24, DOI 10.1080/14686996.2023.2165871.

- [55] Y. Hu, G. Huang, J. Tian, J. Qiu, Y. Jia, D. Feng, Z. Wei, S. Li, F. Xu, *NPG Asia Mater* **2021**, *13*, 35.
- [56] M. A. Skylar-Scott, S. G. M. Uzel, L. L. Nam, J. H. Ahrens, R. L. Truby, S. Damaraju, J. A. Lewis, *Sci Adv* 2019, 5, DOI 10.1126/sciadv.aaw2459.
- [57] S. You, Y. Xiang, H. H. Hwang, D. B. Berry, W. Kiratitanaporn, J. Guan, E. Yao, M. Tang, Z. Zhong, X. Ma, D. Wangpraseurt, Y. Sun, T. Lu, S. Chen, *Sci Adv* **2023**, *9*, DOI 10.1126/sciadv.ade7923.
- [58] P. Rukavina, F. Koch, M. Wehrle, K. Tröndle, G. Björn Stark, P. Koltay, S. Zimmermann, R. Zengerle, F. Lampert, S. Strassburg, G. Finkenzeller, F. Simunovic, *Biotechnol Bioeng* **2020**, *117*, 3902.
- [59] M. Gruene, M. Pflaum, C. Hess, S. Diamantouros, S. Schlie, A. Deiwick, L. Koch, M. Wilhelmi, S. Jockenhoevel, A. Haverich, B. Chichkov, *Tissue Eng Part C Methods* 2011, 17, 973.
- [60] B. Grigoryan, D. W. Sazer, A. Avila, J. L. Albritton, A. Padhye, A. H. Ta, P. T. Greenfield, D. L. Gibbons, J. S. Miller, *Sci Rep* 2021, 11, 3171.
- [61] M. Wang, W. Li, J. Hao, A. Gonzales, Z. Zhao, R. S. Flores, X. Kuang, X. Mu, T. Ching, G. Tang, Z. Luo, C. E. Garciamendez-Mijares, J. K. Sahoo, M. F. Wells, G. Niu, P. Agrawal, A. Quiñones-Hinojosa, K. Eggan, Y. S. Zhang, *Nat Commun* 2022, *13*, 3317.
- [62] Y. Zhang, F. Jiang, Y. C. Zhao, A.-N. Cho, G. Fang, C. D. Cox, H. Zreiqat, Z. F. Lu, H. Lu, L. A. Ju, *Biomedical Materials* **2023**, *18*, 055008.
- [63] K. Ino, H.-J. Pai, K. Hiramoto, Y. Utagawa, Y. Nashimoto, H. Shiku, *ACS Omega* **2021**, *6*, 35476.
- [64] Y. Nashimoto, R. Okada, S. Hanada, Y. Arima, K. Nishiyama, T. Miura, R. Yokokawa, *Biomaterials* **2020**, *229*, 119547.
- [65] W. Streule, T. Lindemann, G. Birkle, R. Zengerle, P. Koltay, *JALA: Journal of the Association for Laboratory Automation* **2004**, *9*, 300.
- [66] C. J. Hunt, Transfusion Medicine and Hemotherapy 2019, 46, 134.

SUPPORTING INFORMATION

Droplet 3D Cryobioprinting for Fabrication of Free-Standing and Volumetric Structures

Joshua Weygant,¹ Ali Entezari,[†] Fritz Koch,[†] Ricardo André Galaviz,[†] Carlos Ezio Garciamendez, Pável Hernández, Vanessa Ortiz, David Sebastián Rendon Ruiz, Francisco Aguilar, Andrea Andolfi, Ling Cai, Sushila Maharjan, Anayancy Osorio, Yu Shrike Zhang^{*}

J. Weygant, Dr. F. Koch, R.A. Galaviz, Dr. A. Entezari, C. E. Garciamendez, P. Hernández, V. Ortiz, D. S. Rendón Ruiz, F. Aguilar, A. Andolfi, L. Cai, Dr. S. Maharjan, Prof. Y. S. Zhang Division of Engineering in Medicine, Department of Medicine, Brigham and Women's Hospital, Harvard Medical School, Cambridge, MA 02139, USA

*Email: yszhang@bwh.harvard.edu

Dr. F. Koch, Prof. A. Osorio

Laboratory for Bioinspired Materials for Biomedical Engineering, IMTEK - Department of Microsystems Engineering, University of Freiburg, 79110 Freiburg, Germany

Dr. A. Entezari

School of Biomedical Engineering, University of Technology Sydney, NSW, 2007, Australia

A. Andolfi

Department of Informatics, Bioengineering, Robotics and Systems Engineering (DIBRIS), University of Genova, Genova, Italy

[†]A. Entezari, F. Koch, and R. A. Galaviz contributed to this work equally

¹J. Weygant is now at the Department of Engineering, University of Cambridge, CB2 1PZ Cambridge, United Kingdom

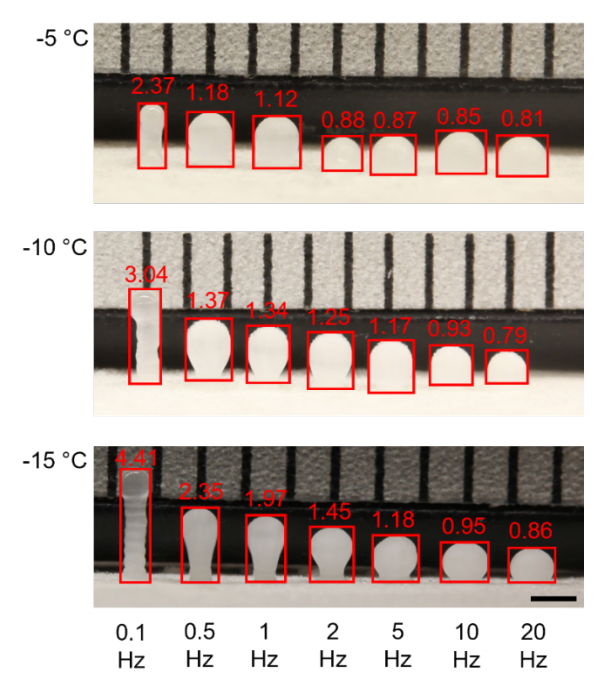


Figure S1. Representative images of printed pillars to assess the achievable aspect ratio of structures fabricated *via* cryo-droplet printing at -5 °C, -10 °C, and -15 °C. Objects were printed by dispensing droplets onto the same spot for different frequencies (0.1-20 Hz). n=5 prints were conducted for each temperature and the aspect ratio was calculated by dividing the height of the structure by the width at the widest point. For each structure, the aspect ratio is exemplary shown as well. Scale bar: 1 mm.

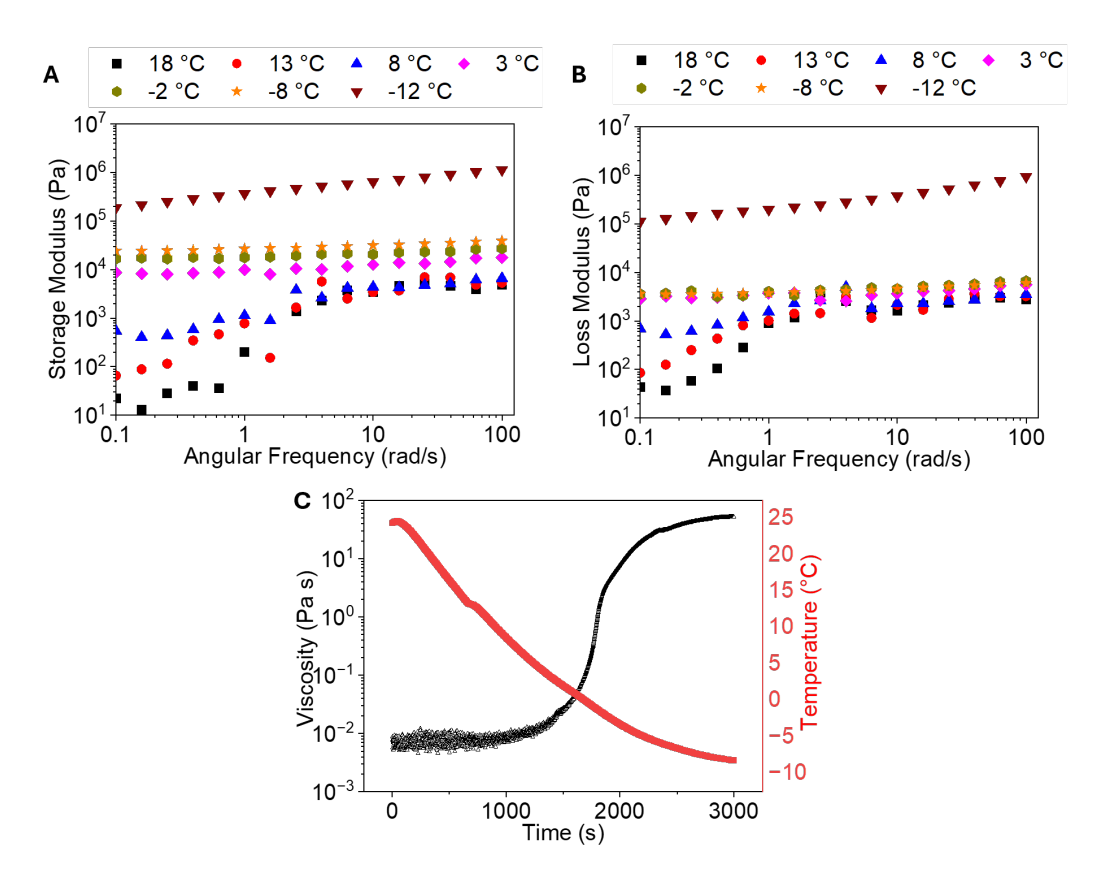


Figure S2. Influence of temperature on viscoelastic properties on the used GelMA derived from fish skin. (A, B) Storage and loss moduli for a temperature sweep with increasing angular frequencies. (C) Influence of temperature on viscosity.

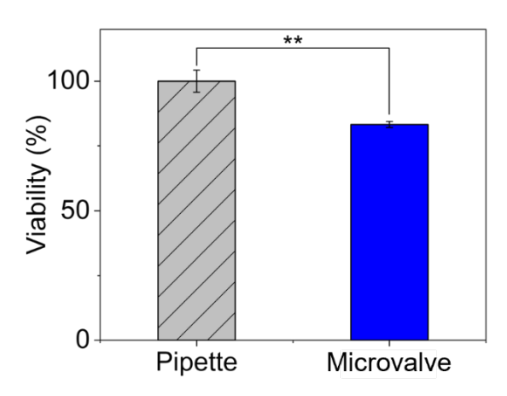


Figure S3. Viability of pipetted C2C12 cells compared to viability of C2C12 cells bioprinted via microvalve. Results are normalized to viability of pipetted cells. n=3; **p<0.001.

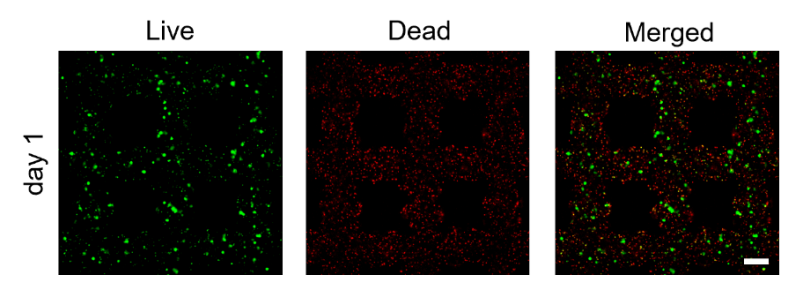


Figure S4. Representative fluorescence live (green) and dead (red) images of C212 cells bioprinted onto the cryoplate that was cooled to -15 $^{\circ}$ C and yielded a cell viability of 12±7% on day 1. Scale bar: 500 μ m.

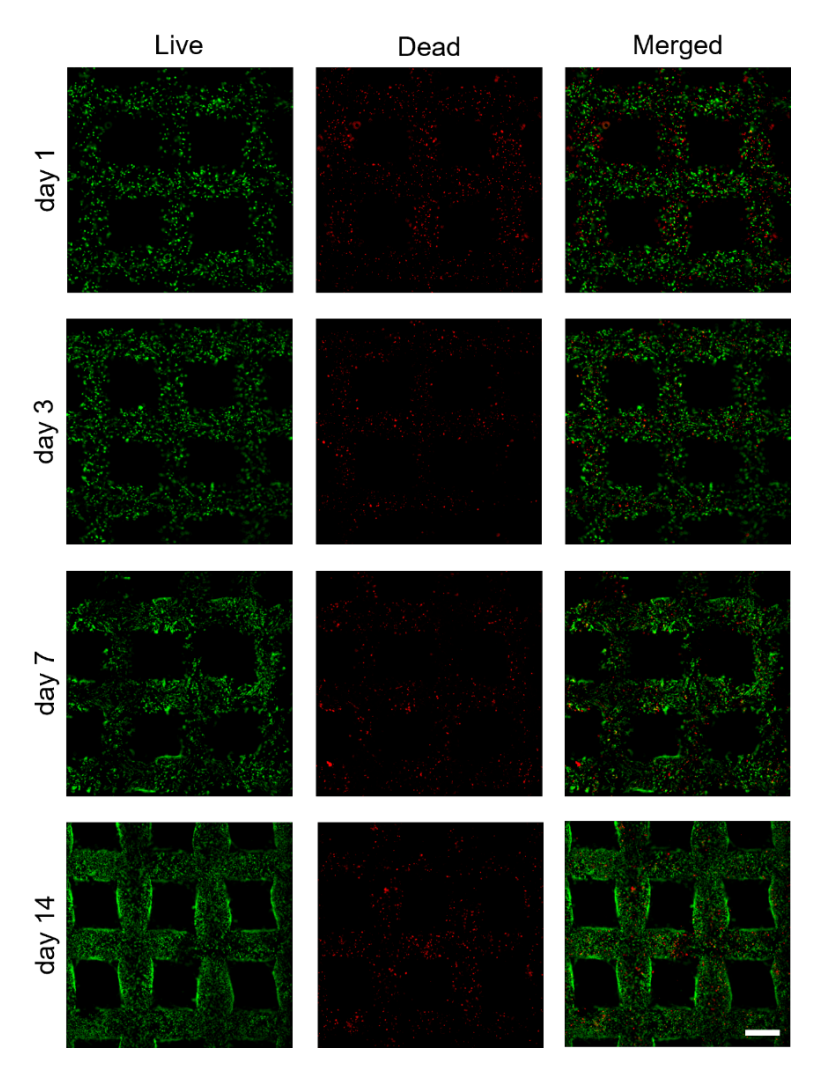


Figure S5. Representative fluorescence live (green) and dead (red) images of C212 cells bioprinted onto the cryoplate that was cooled to -10 $^{\circ}$ C at days 1, 3, 7, and 14. Scale bar: 500 μ m.

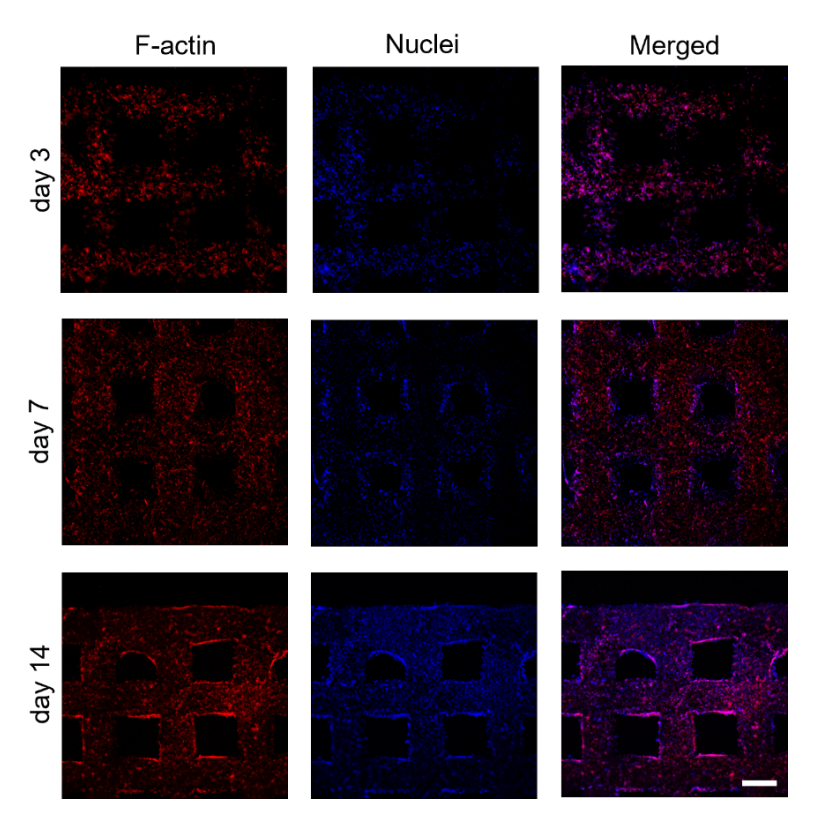


Figure S6. Representative fluorescence images of C2C12 cells stained for F-actin (red) and nuclei (blue) to visualize their morphologies. Grids were bioprinted onto the cryoplate that was cooled to -5 $^{\circ}$ C. Scale bar: 500 μ m.

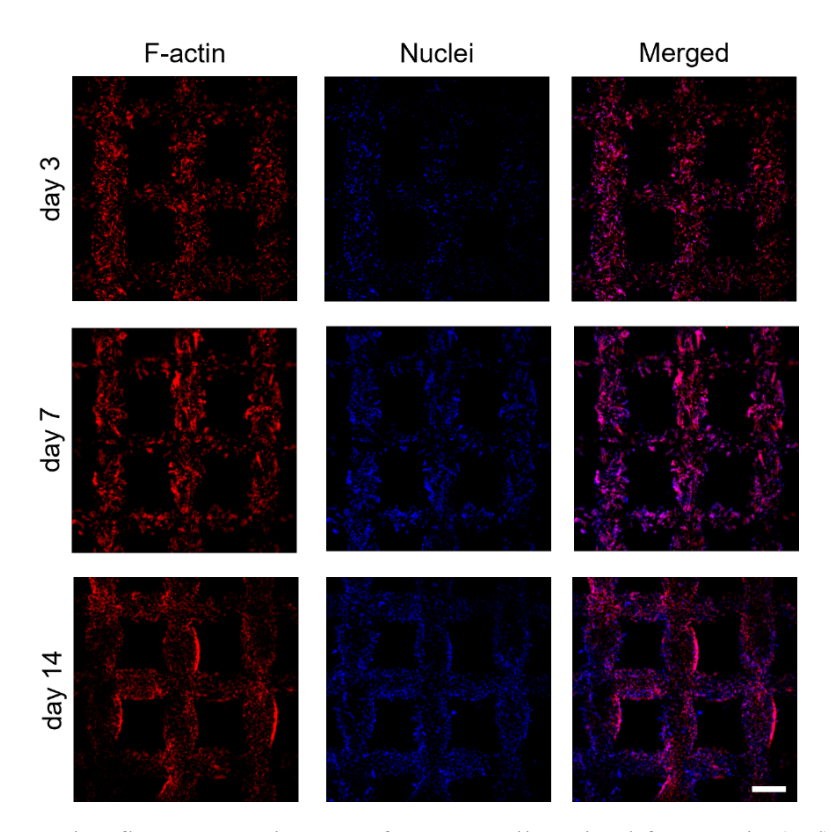


Figure S7. Representative fluorescence images of C2C12 cells stained for F-actin (red) and nuclei (blue) to visualize their morphologies. Grids were bioprinted onto the cryoplate that was cooled to -10 $^{\circ}$ C. Scale bar: 500 μ m.

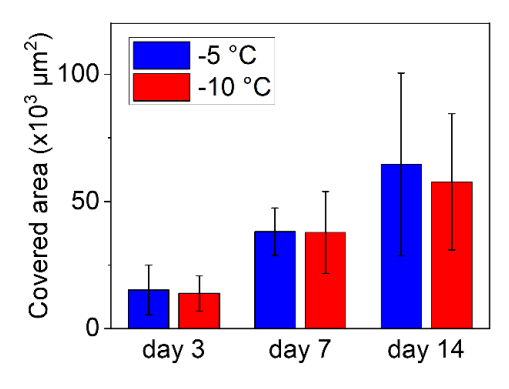


Figure S8. Quantification of areas covered by C2C12 cells that were bioprinted onto the cryoplate that was set to either -5 or -10 °C. Constructs were analyzed on days 3, 7, and 14. $n\ge 2$.

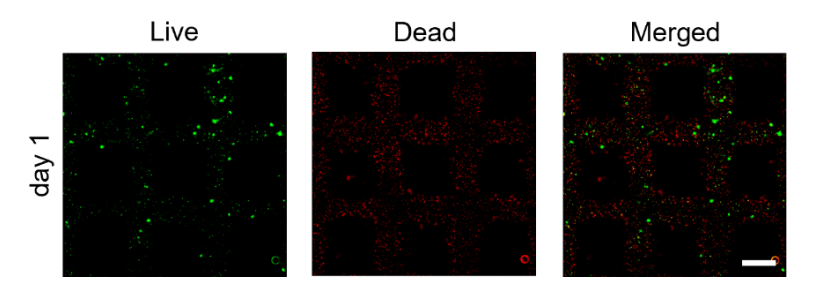


Figure S9. Representative fluorescence live (green) and dead (red) images of NIH/3T3 cells bioprinted onto the cryoplate that was cooled to -15 $^{\circ}$ C and yielded a cell viability of 19±7% on day 1. Scale bar: 500 μ m; n=3.

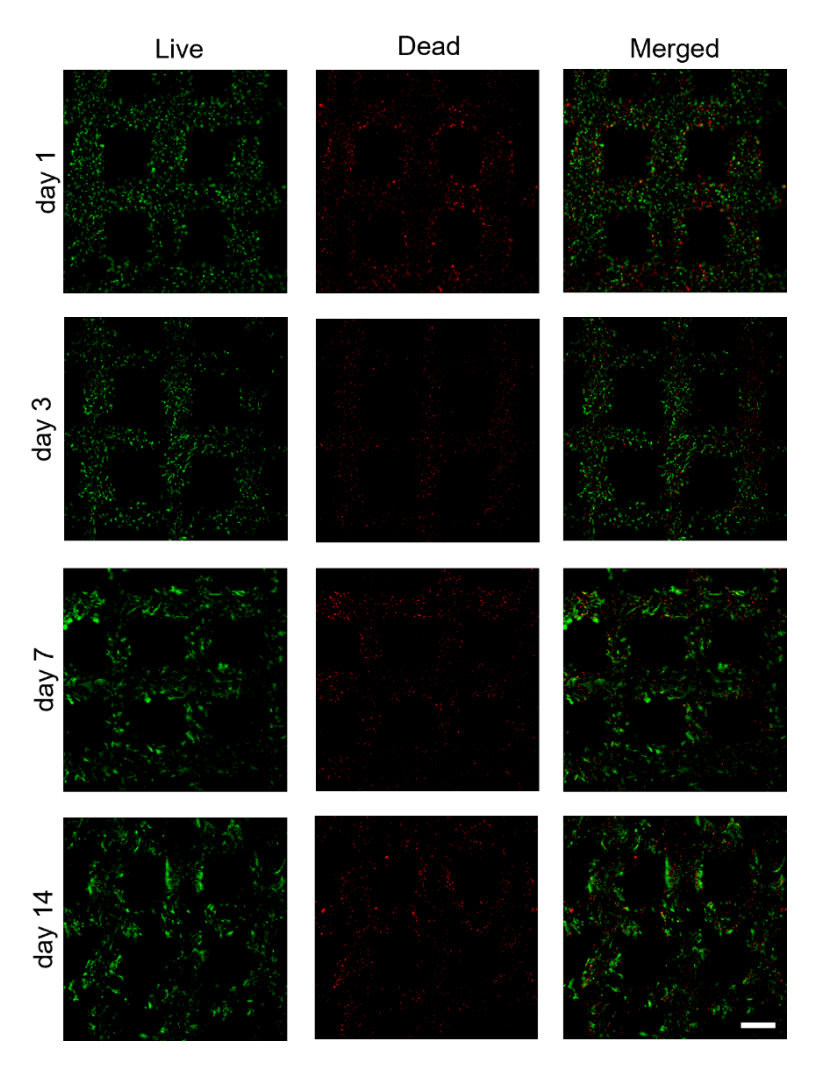


Figure S10. Representative fluorescence live (green) and dead (red) images of NIH/3T3 cells bioprinted onto the cryoplate that was cooled to -10 $^{\circ}$ C at days 1, 3, 7, and 14. Scale bar: 500 μ m.

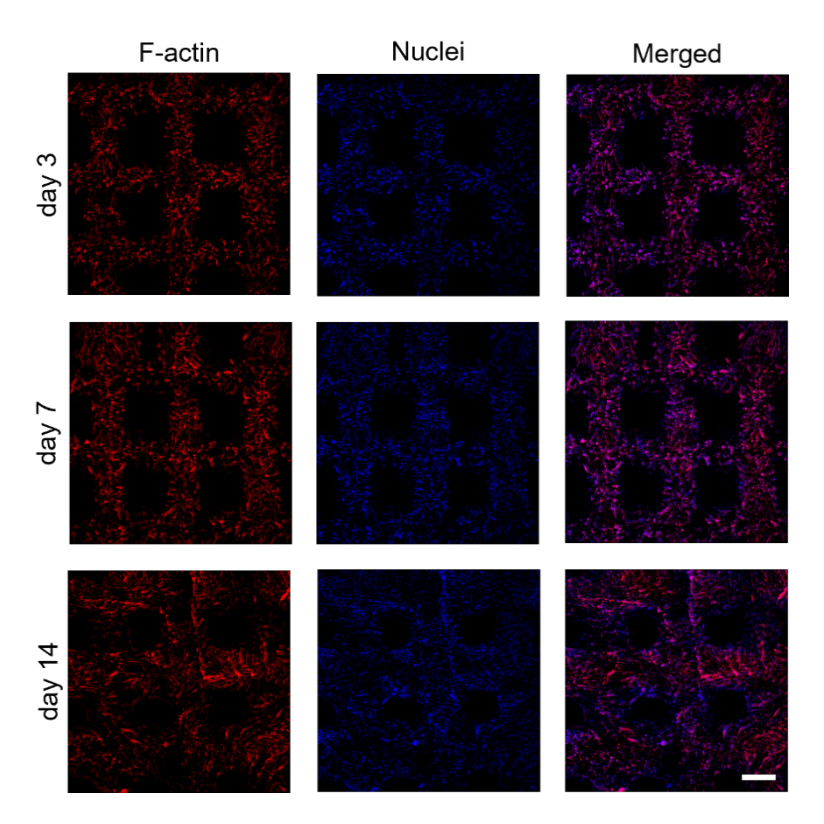


Figure S11. Representative fluorescence images of NIH/3T3 cells stained for F-actin (red) and nuclei (blue) to visualize their morphologies. Grids were bioprinted onto the cryoplate that was cooled to -5 °C. Scale bar: $500 \ \mu m$.

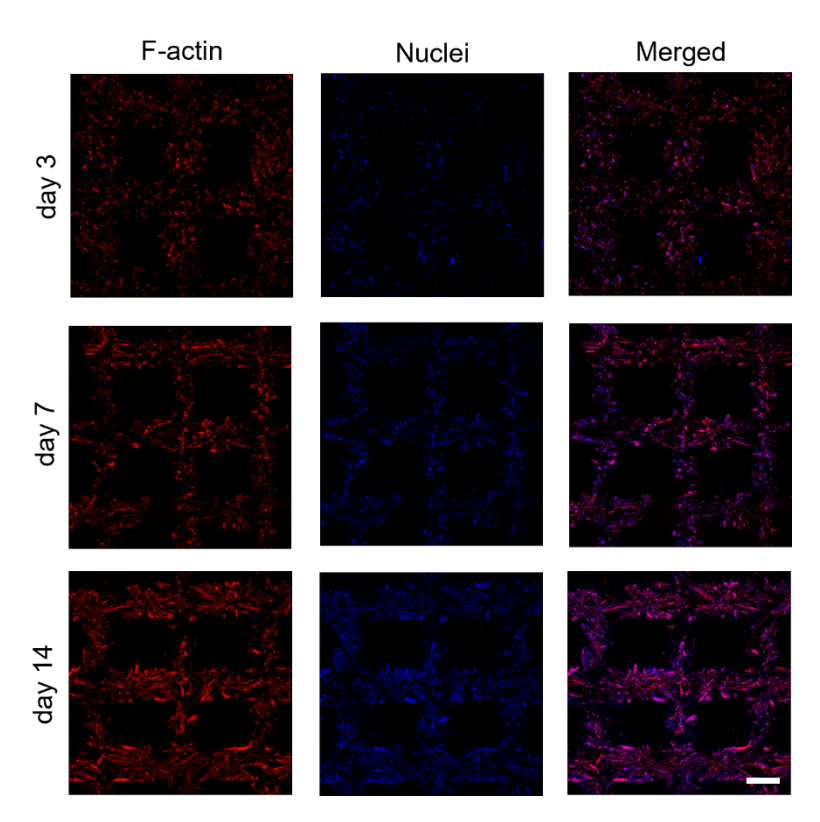


Figure S12. Representative fluorescence images of NIH/3T3 cells stained for F-actin (red) and nuclei (blue) to visualize their morphologies. Grids were bioprinted onto the cryoplate that was cooled to -10 $^{\circ}$ C. Scale bar: 500 μ m.

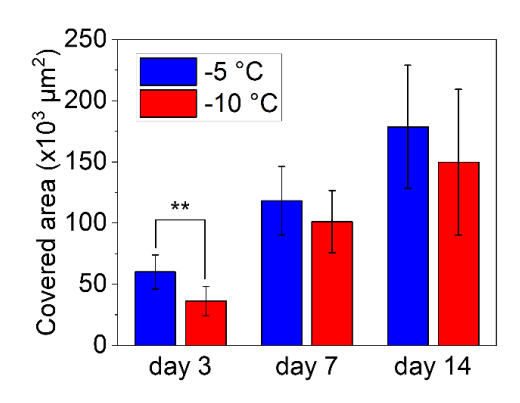


Figure S13. Quantification of areas covered by NIH/3T3 cells that were bioprinted onto the cryoplate that was set to either -5 or -10 °C. Constructs were analyzed on days 3, 7, and 14. n=3; **p<0.001.

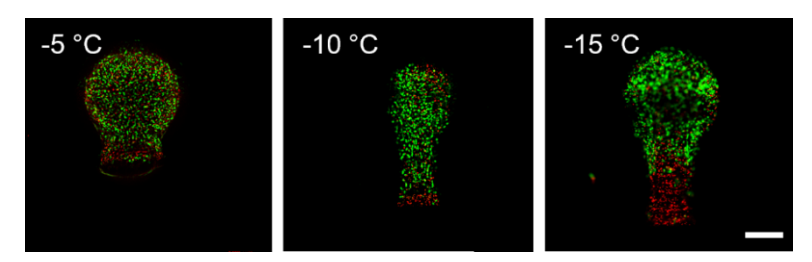


Figure S14. Representative fluorescence live (green) and dead (red) images of C212 cells that were bioprinted as pillars onto the cryoplate that was cooled to -5, -10, and -15 $^{\circ}$ C. Scale bar: 500 μ m.

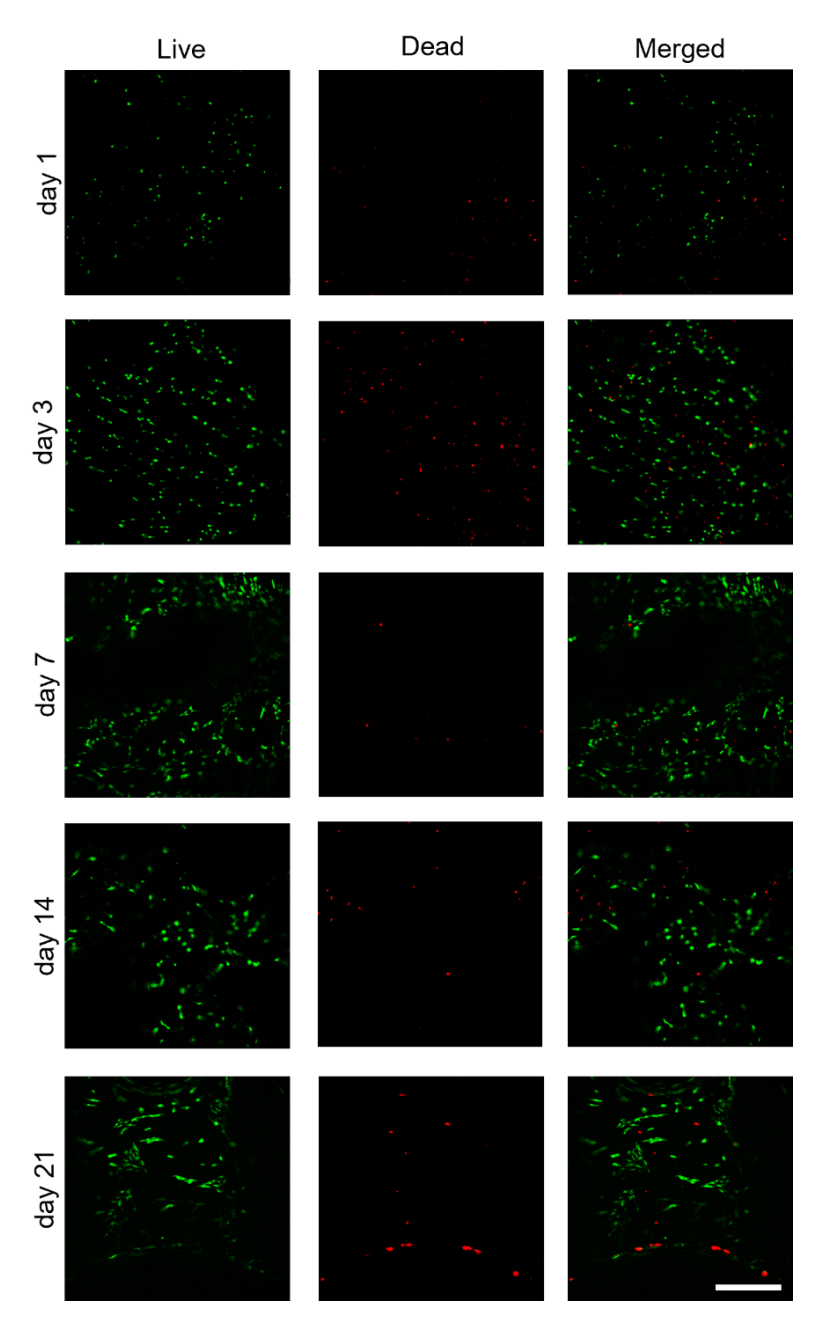


Figure S15. Representative fluorescence live (green) and dead (red) images of HUVECs bioprinted onto the cryoplate that was cooled to -5 °C at days 1, 3, 7, 14, and 21. Scale bar: 200 μm .

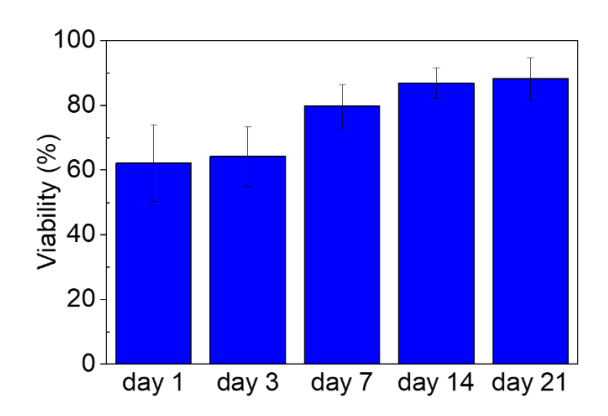


Figure S16. Quantification of viabilities of HUVECs bioprinted onto the cryoplate that was cooled to °C on days 1, 3, 7, 14, and 21. n=3.

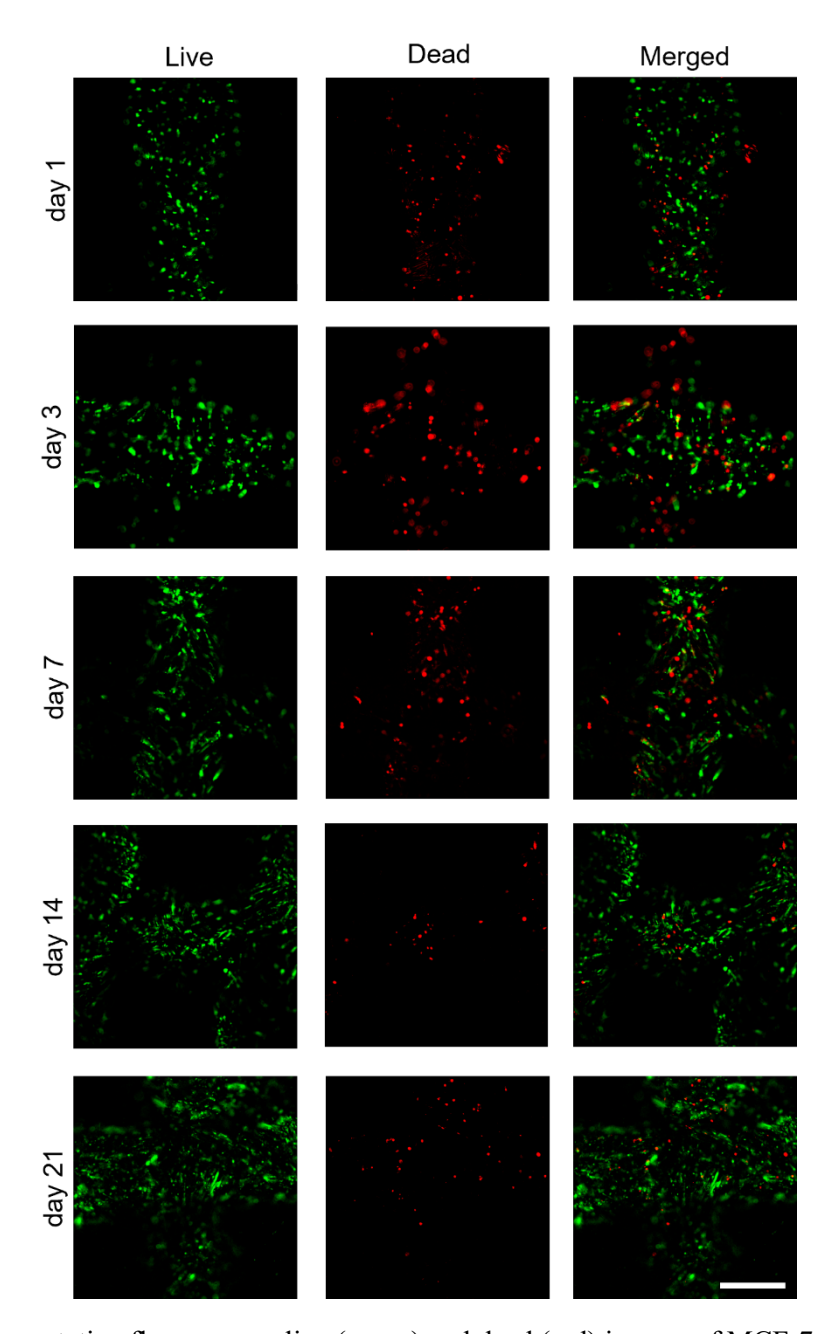


Figure S17. Representative fluorescence live (green) and dead (red) images of MCF-7 cells bioprinted onto the cryoplate that was cooled to -5 $^{\circ}$ C at days 1, 3, 7, 14, and 21. Scale bar: 200 μ m.

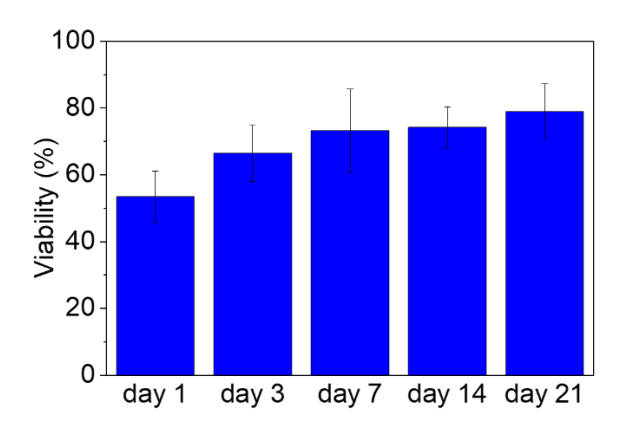


Figure S18. Quantification of viabilities of MCF-7 cells bioprinted onto the cryoplate that was cooled to 5 °C on days 1, 3, 7, 14 and 21; n=3.